The 2013 M_w 6.2 Khaki-Shonbe (Iran) Earthquake: Insights into seismic and aseismic shortening of the Zagros sedimentary cover

J. R. Elliott[1], E. A. Bergman[2], A. C. Copley[3], A. R. Ghods[4], E. K. Nissen[5], B. Oveisi[6], M. Tatar[7], R. J. Walters[8], and F. Yamini-Fard[7]

[1]COMET+, Department of Earth Sciences, University of Oxford, Oxford, UK, [2]Center for Imaging the Earth's Interior, Department of Physics, University of Colorado Boulder, Boulder, Colorado, USA, [3]COMET+, Department of Earth Sciences, Bullard Laboratories, Cambridge, UK, [4]Department of Earth Sciences, Institute for Advanced Studies in Basic Sciences, Zanjan, Iran, [5]Department of Geophysics, Colorado School of Mines, Golden, Colorado, USA, [6]Seismotectonics Department, Geological Survey of Iran, Tehran, Iran, [7]International Institute of Earthquake Engineering and Seismology, Tehran, Iran, [8]COMET+, School of Earth and Environment, University of Leeds, Leeds, UK

Abstract Determining the relationship between folding and faulting in fold and thrust belts is important for understanding the growth of geological structures, the depth extent of seismic slip, and consequently, the potential earthquake hazard. The 2013 M_w 6.2 Khaki-Shonbe earthquake occurred in the Simply Folded Belt of the Zagros Mountains, Iran. We combine seismological solutions, aftershock relocations, satellite interferometry, and field observations to determine fault geometry and its relationship with the structure, stratigraphy, and tectonics of the central Zagros. We find reverse slip on two along-strike, southwest dipping fault segments. The main shock rupture initiated at the lower northern end of the larger northwest segment. Based upon the hypocenter and rupture duration, slip on the smaller southern segment is likely aseismic. Both faults verge away from the foreland, toward the high-range interior, contrary to the fault geometries depicted in many structural cross sections of the Zagros. The modeled slip occurred over two mutually exclusive depth ranges above 10 km, resulting in long (~16 km), narrow rupture segments (~7 km). Aftershocks cluster in the depth range 3–14 km. This indicates reverse slip and coseismic shortening occurred mostly or exclusively in the sedimentary cover, with slip distributions likely to be lithologically controlled in depth by the Hormuz salt at the base of the sedimentary cover (~10–12 km), and the Kazhdumi Formation mudrocks at upper levels (~4–5 km). Our findings suggest lithology plays a significant role in the depth extent of slip found in reverse faults in folded belts, providing an important control on the potential size of earthquakes.

1. Introduction

On 9 April 2013 (11:53 UTC, 16:23 local time) a M_w 6.2 earthquake struck the Zagros Simply Folded Belt in southwestern Iran (Figure 1). The epicenter was 20 km northeast of the town of Khaki, and the earthquake resulted in 40 fatalities [*Daniell et al.*, 2011], mainly in the village of Shonbe 20 km southeast of the epicenter. The largest aftershock (M_w 5.4) was 14 hours later, and a series of 91 teleseismically and regionally recorded (M_w 3.5–5.4) and 1350 locally recorded (M 1–5) aftershocks occurred over the following month.

We provide a combined seismotectonic analysis of the Khaki-Shonbe earthquake using observations from seismology and aftershock relocations, synthetic aperture radar interferometry (InSAR), field measurements of surface deformation, and satellite imagery (Figure 1). The source mechanism and centroid depth are determined with body waveform modeling, while the fault location, geometry, and distribution of slip are constrained by the InSAR displacements. Improved epicentral relocations of 176 (M_w 3.5–6.2) earthquakes up until the end of 2013 (66 of which were prior to the main shock in April, from 1966 onward) were performed to determine locations of the larger aftershocks, resolve the InSAR focal plane ambiguity, and determine the rupture propagation direction. Just over 55 h before the main shock, a M 3.9 earthquake occurred at the same epicentral location (within uncertainties) of the impending M_w 6.2 epicenter. Additionally, a dense local seismometer network was deployed 5 days after the main shock for a period of 1 month, locating 1350 magnitude 1–5 events.
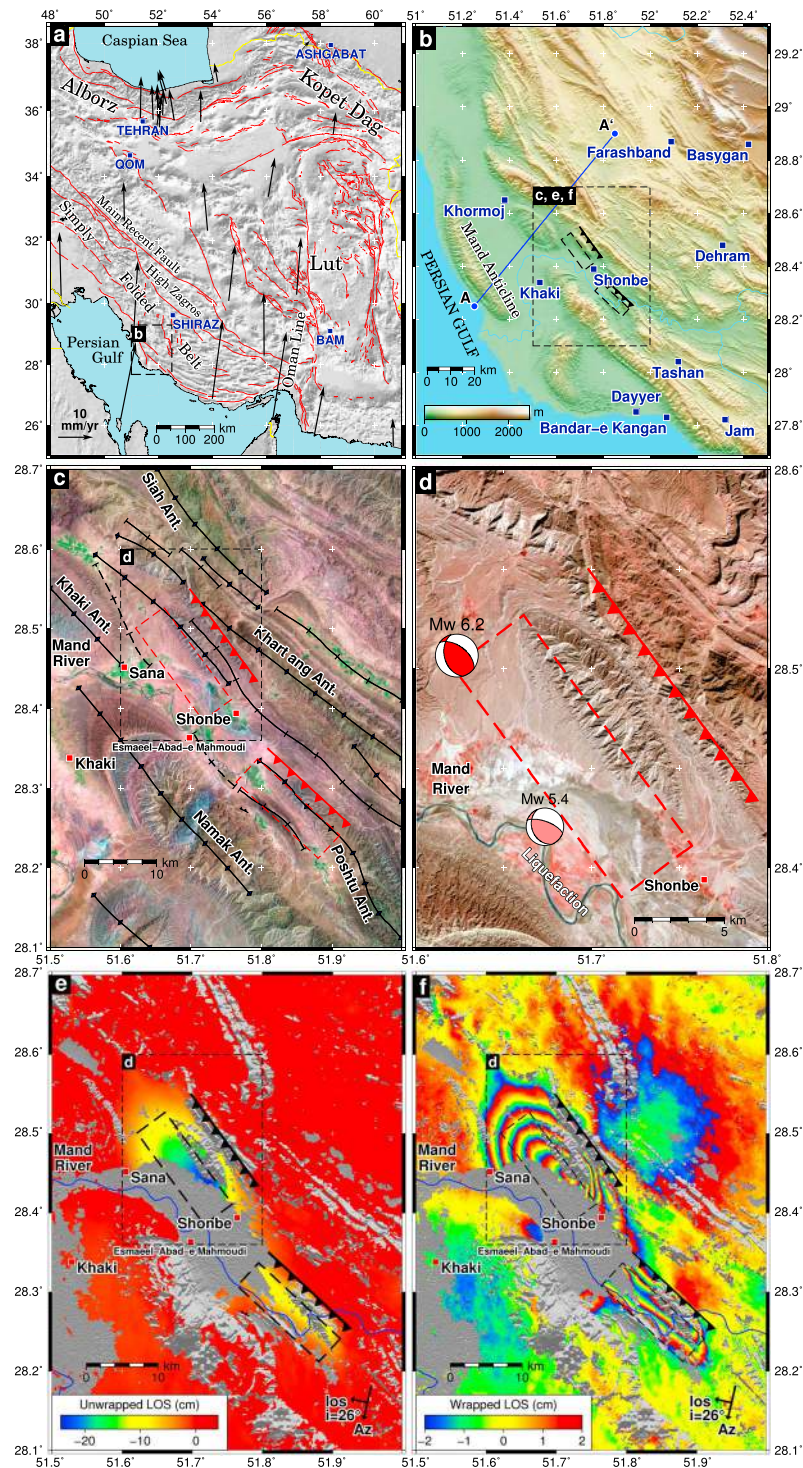
Figure 1. (a) GPS velocities of Iran with respect to Eurasia [*Reilinger et al.*, 2006]. Major faults are denoted in red from *Walker et al.* [2013a]. (b) Topography of the SW Zagros with major towns and villages marked. Structural cross section through A–A' is shown in Figure 3. (c) Landsat mosaiced Enhanced Thematic Mapper (ETM) image (RGB 742) with anticlines and synclines from *Oveisi et al.* [2009] denoted in black. The surface projections of our preferred interpretation of southwestward dipping fault segments from this study are shown in red. Field observations of surface fractures in the locality of N28.2704°E51.778944° in the hanging wall of the SE segment are marked by a thin black barbed line. (d) ASTER image (RGB 321) of the NW segment (red line), north of Shonbe, with body waveform solutions shown in red. (e) Unwrapped RADARSAT-2 interferogram (12 October 2012 to 23 April 2013) showing peak motion toward the satellite of 25 cm and the updip projections of the faults to the surface in black. (f) Wrapped version (4 cm contours) of the interferogram showing the two lobes of deformation corresponding to the NW and SE fault segments.
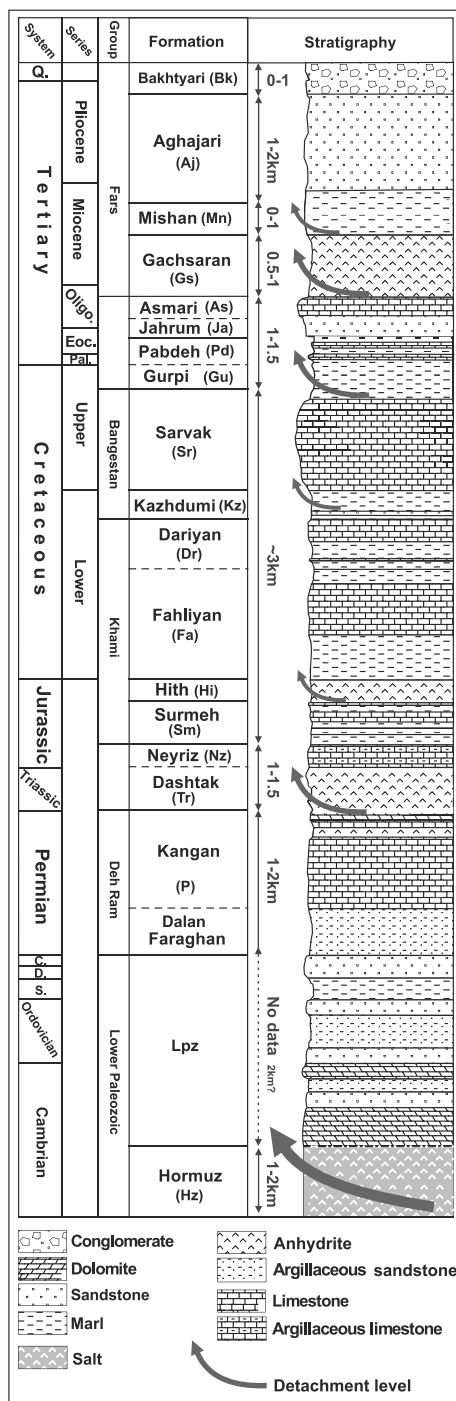
Figure 2. Stratigraphic column modified from *Oveisi et al.* [2009] for this region of the Zagros indicating the various lithologies and potential detachment levels within the sedimentary succession. Estimates of the range of thicknesses of the layers are also given, based upon *Sherkati et al.* [2006].

This is the largest earthquake in the Zagros since the November 1990 M_w 6.4 Furg (Hormozgan) reverse faulting event [*Walker et al.*, 2005], and therefore, the largest in the period for which dense InSAR ground displacements are available. It is also the biggest seismic event to have occurred in the Simply Folded Belt since the March 1977 M_w 6.7 Khurgu earthquake [*Berberian and Papastamatiou*, 1978]. This earthquake therefore potentially provides valuable insights into a range of regional controversies: (1) the preponderance of earthquake faulting in the crystalline basement versus the sedimentary cover and the potential importance of lithology in controlling and limiting seismic rupture [e.g., *Talebian and Jackson*, 2004; *Nissen et al.*, 2011; *Copley et al.*, 2015], (2) the nature of surface folding and whether or not there is a one-to-one relationship between buried reverse faults and surface anticlines [e.g., *Berberian*, 1995; *McQuarrie*, 2004; *Mouthereau et al.*, 2007], and (3) the presence or absence of large pulses of aseismic slip triggered by main shock rupture [*Barnhart et al.*, 2013; *Nissen et al.*, 2014]. Therefore, to test these ideas, we compare the depth extent and surface expression of buried, coseismic fault slip with the surface observations, locations of aftershocks, and local geology including likely stratigraphic depths and long-term uplift expressed in folding.

2. Tectonic Setting of the Zagros

The Zagros mountains are a key element within the continental collision between the Arabian and Eurasian plates, which began between 35 Ma and 20 Ma [*Allen and Armstrong*, 2008; *Mouthereau et al.*, 2012; *McQuarrie and van Hinsbergen*, 2013]. Decadal N-S shortening rates measured with GPS (Figure 1a) range from ~9 mm/yr across the SE Zagros to ~4 mm/yr across the NW Zagros [*Vernant et al.*, 2004], making up roughly one third of the total Arabia-Eurasia convergence rate. This shortening is perpendicular to the E-W trend of the SE Zagros but oblique to the NW-SE trend of the NW Zagros, where slip partitioning results in right-lateral motion along the Main Recent Fault [*Talebian and Jackson*, 2004]. Present day deformation is concentrated within the lower part of the range, known as the Simply Folded Belt (SFB) [*Talebian and Jackson*, 2004; *Walpersdorf et al.*,

2006]. This region (Figure 1a) is structurally distinct from the High Zagros, which appears no longer active except for the Main Recent Fault, parts of the High Zagros Fault zone, and along the Oman Line [e.g., *Talebian and Jackson*, 2004; *Walker et al.*, 2005].

The SFB contains a thick, folded sedimentary cover which records deposition on the Arabian passive margin across much of the Phanerozoic (Figure 2). Within parts of the southeastern SFB, including our study
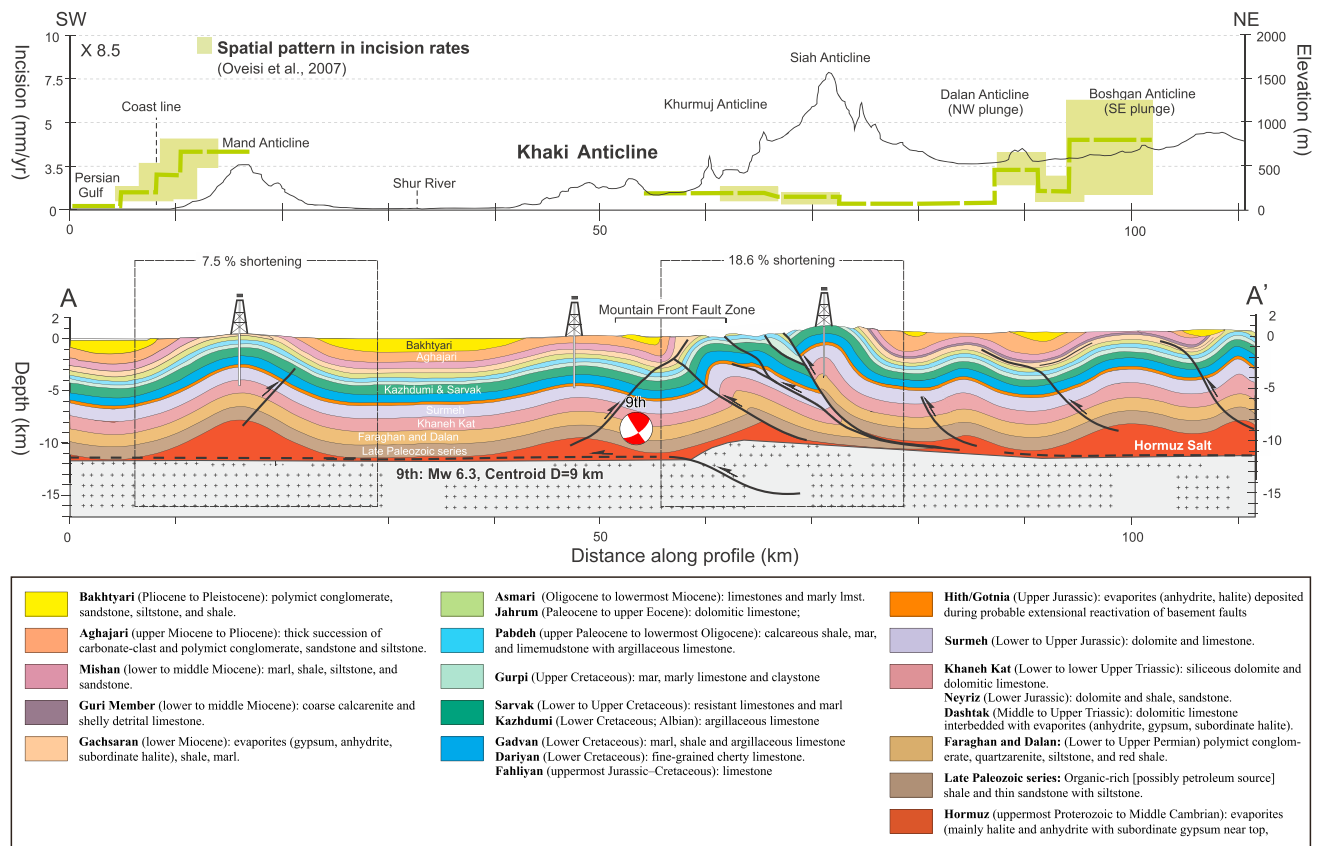
Figure 3. Structural cross section modified from *Oveisi et al.* [2009] (updated from *Sherkati et al.* [2006]) showing the faulting, anticlines, and position of the main shock (red focal mechanism) projected 4 km NW along strike onto the line of section. See Figure 2 for lithologies and ages. The position of the section is shown in Figures 1b and 4. The Hormuz salt is at 10–12 km depth in the Khaki region, with basement below. The incision rates are from *Oveisi et al.* [2007].

area, these sediments are detached from underlying basement rocks by late Precambrian-Cambrian Hormuz Formation evaporites which are exposed at the surface within numerous diapirs [e.g., *Kent*, 1979; *Jahani et al.*, 2007]. The original thickness of the Hormuz salt may have been a few kilometers, although presumably much is now removed through diapirism and erosion. Above the salt, platform carbonates and clastic rocks of the lower cover are only rarely exposed within the SFB and are mostly known from the High Zagros. Their thicknesses, and that of the cover as a whole, are consequently quite poorly constrained. Nevertheless, they are thought to behave structurally as a single, strong layer termed the 'Competent Group' [*O'Brien*, 1957]. The middle cover comprises further strong platform carbonates, interbedded with weaker marls, shales, and evaporites, some of which are thought to form regional décollements [e.g., *Shen et al.*, 2005; *Sepehr et al.*, 2006; *Yamato et al.*, 2011]. The upper cover comprises Miocene-Recent sandstones and conglomerates, marking the onset of continental shortening, uplift, and erosion [*Hessami et al.*, 2001b; *Fakhari et al.*, 2008; *Khadivi et al.*, 2010].

There is considerable uncertainty both over the total thickness of cover rocks and the means by which they are shortened. In the absence of published, onshore seismic reflection profiles, balanced cross sections (Figure 3) provide the best constraints on cover thickness, generally supporting depths-to-basement of ∼8–12 km [e.g., *McQuarrie*, 2004; *Molinaro et al.*, 2005; *Sherkati et al.*, 2006; *Mouthereau et al.*, 2007; *Oveisi et al.*, 2009; *Allen et al.*, 2013]. Outcrops and borehole data in particular, provide a good thickness control on Permian to recent sedimentary units, but thicknesses of deeper horizons are more uncertain. However seismic reflection profiles in the Persian Gulf indicate cover thicknesses of as much as ∼14 km [*Jahani*, 2008; *Jahani et al.*, 2009; *Perotti et al.*, 2011]. Cover rocks are folded into arrays of concentric anticlines and synclines with characteristic "whaleback" shapes expressed in hard units such as the Asmari Limestone. These are usually depicted as
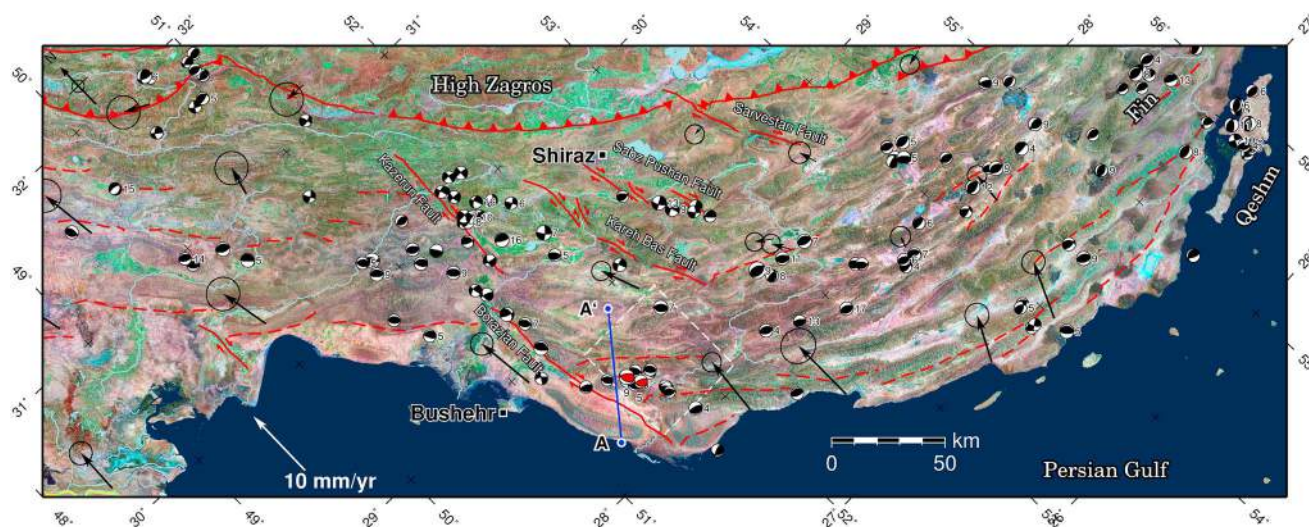
Figure 4. Map of the Zagros depicting the locations of past earthquakes and focal mechanisms from *Nissen et al.* [2011], overlaid on a Landsat ETM mosaic (RGB 742). Numbers next to focal mechanisms indicate centroid depths (km) calculated from body waveform solutions. The body waveform solutions for the main shock on the 9 April and the largest aftershock on the 10 April are shown in red. GPS vectors are velocities with respect to the Iran Central Block from *Walpersdorf et al.* [2006], and uncertainty ellipses are the 95% confidence interval. Inferred blind, basement reverse faults are denoted in dashed red and are from *Berberian* [1995]. The profile line A–A' shown in Figure 3 runs 5 km to the NW of the Khaki earthquake and is shown in blue. The white dashed box marks the extents of Figure 6.

detachment folds formed by buckling of strata over a décollement (Figure 3), either within the Hormuz Formation [e.g., *Colman-Sadd*, 1978; *Mouthereau et al.*, 2007] or within certain weak units in the middle cover (Figure 2) such as the Early Miocene Gachsaran evaporites [*Carruba et al.*, 2006; *Sherkati et al.*, 2006; *Casciello et al.*, 2009]. However, some anticlines are alternatively interpreted as fault-propagation folds whose growth is driven by slip on underlying reverse faults [e.g., *McQuarrie*, 2004; *Allen et al.*, 2013], or as fault-bend folds resulting from ramp-and-flat geometries [e.g., *Burberry et al.*, 2008; *Barnhart and Lohman*, 2013]. The former may include a small number of distinctive, asymmetric anticlines which contain rare exposures of Paleozoic strata in their cores [*Berberian*, 1995; *Nissen et al.*, 2011].

The seismicity of the region (Figure 4) is dominated by reverse faulting earthquakes with steep, ~30–60° dips [e.g., *Jackson*, 1980]. Most teleseismically recorded earthquakes have moderate magnitudes of $M_w \leq 6$ and the largest two, at Ghir and Khurgu in the 1970s, were M_w 6.7 [*Jackson and Fitch*, 1981; *Baker et al.*, 1993]. Summed teleseismic moment tensors can only account for a small percentage of the shortening measured with GPS [*Jackson and McKenzie*, 1988; *Masson et al.*, 2005]. In the absence of large ($M > 7$) earthquakes in the ~1000 year historical record [*Ambraseys and Melville*, 1982], this appears to confirm the primary role of aseismic shortening, whether by folding or otherwise. Mapped surface faulting is rare, and no earthquake in the SFB is known to have generated primary surface ruptures (the 1990 Furg earthquake rupture is situated within the High Zagros) [*Walker et al.*, 2005]. As a consequence, earthquakes in the SFB are often assumed to occur mostly, or even exclusively, within the basement. Some of the largest ones lie close to steps of a few kilometers in surface stratigraphic level, attributed to "master blind thrusts" in the basement [*Berberian*, 1995]. Smaller earthquakes detected in a series of local microseismic experiments also tend to be concentrated at basement depths [e.g., *Hatzfeld et al.*, 2003; *Tatar et al.*, 2004; *Nissen et al.*, 2010; *Roustaei et al.*, 2010; *Nissen et al.*, 2011; *Yaminifard et al.*, 2012].

However, teleseismic body waveform modeling places most moderate magnitude (M_w 5–6) reverse-faulting earthquakes in the SFB at depths of 4–10 km, more consistent with rupture in the cover [*Talebian and Jackson*, 2004; *Adams et al.*, 2009; *Nissen et al.*, 2011]. Clear InSAR signals observed in a few recent earthquakes also support coseismic slip at middle or lower cover depths [*Lohman and Simons*, 2005a; *Nissen et al.*, 2007b; *Lohman and Barnhart*, 2010; *Barnhart et al.*, 2013], including two instances in which subsequent microseismic aftershocks clustered within the basement [*Nissen et al.*, 2010; *Roustaei et al.*, 2010]. Together, these results imply that larger earthquakes are concentrated within the middle lower cover, possibly within "Competent Group" sediments [*Nissen et al.*, 2011]. This interpretation was recently challenged by *Barnhart and Lohman* [2013], who suggested that the InSAR signals reflected triggered pulses of aseismic slip and that the initial main

shocks occurred within the basement. However, their model is inconsistent with teleseismic body waveform modeling which confirms that main shock seismic slip was centered at shallower depths [*Nissen et al.*, 2014].

Strike-slip faulting also plays an important role in the central SFB, where five major, N-S trending, right-lateral faults have been mapped on the basis of earthquake focal mechanisms and offsets to surface folding [*Baker et al.*, 1993; *Hessami et al.*, 2001a; *Authemayou et al.*, 2006, 2009]. These faults—from W to E (Figure 4), the Borazjan, Kazerun, Kareh Bas, Sabz Pushan, and Sarvestan faults—are thought to rotate anticlockwise about vertical axes, thereby accommodating along-strike extension between the southeastern and northwestern SFB [*Talebian and Jackson*, 2004]. Our study area lies just east of the Borazjan fault.

3. The Seismology of The Khaki Earthquake Sequence

We analyze the seismology of the Khaki earthquake sequence with three distinct approaches over differing timescales to capture the various spatial-temporal relationships between the main shock and aftershocks: (1) relocated hypocenters of regional and teleseismically recorded seismicity in the period 1966–2013, (2) locally recorded aftershock microseismicity in the month following the Khaki earthquake, and (3) body wave analysis of teleseismic waveforms to determine the focal parameters of the Khaki main shock and largest aftershock.

3.1. Earthquake Relocations
3.1.1. Location Calibration

Calibrated relocations allow us to determine accurate hypocenters for events not recorded by the month-long local aftershock deployment, including the main shock itself. The approach used to obtain calibrated locations for the Khaki sequence, using regional and teleseismically recorded phases for the period 1966–2013 (mainly 1999–onward), is identical to that used in many prior studies [*Ghods et al.*, 2012; *Zanjani et al.*, 2013; *Walker et al.*, 2013a, 2013b; *McNamara et al.*, 2014, and references therein]. Relative locations of the events in a cluster (spanning a limited area but unrestricted in time) are constrained using the program *mloc*, based on the Hypocentroidal Decomposition (HD) method of *Jordan and Sverdrup* [1981] with extensive development since its original applications to reduce location bias of the absolute locations. We refer to locations in which location bias has been substantially reduced and for which realistic estimates of uncertainty have been obtained as "calibrated." The level of calibration that can achieved for any given set of earthquakes depends critically on the nature of the arrival time data set that is available, i.e., the distribution of stations, the quantity, and quality of arrival time picks, and also on the level of heterogeneity in the crustal velocity structure in the source region. Experience in Iran and many other locales around the world indicates that location accuracies of several kilometers are often achievable and subkilometer accuracy can be achieved under especially favorable conditions. The uncertainties of our analysis of the Khaki sequence are discussed later.

The relocation process in HD is separated into two parts. The first part is the estimation of improved "cluster vectors" that describe the relative locations (in space and time) of all events with respect to a reference point called the hypocentroid, defined as the arithmetic mean of individual event hypocenters. Estimation of the cluster vectors is normally done using data from all phases at all distances because this estimation process is based on arrival time differences and is therefore immune to problems with the theoretical traveltimes. Estimation of the hypocentroid itself is the second part of the two-step process, which is iterated several times to convergence. The problem of calibration of a cluster of earthquakes mainly resolves around the issue of determining a hypocentroid that is not biased.

Location bias in earthquake location algorithms arises primarily from the fitting of arrival time data to theoretical traveltimes that depart significantly from the true (but unknown) traveltimes in the Earth. The problem is especially severe for seismicity that is recorded (as in Iran) mainly by regional seismograph networks observing Pn as the first arrival. Variations in crustal thickness introduce substantial variations in the true traveltime of Pn, which are mapped into location bias through the geometry of observing stations convolved with an assumed 1-D velocity model. Previous work (see above references) has shown that location bias of 20 km is not uncommon in Iran.

The key to obtaining calibrated locations with *mloc* lies in the selection of data with which to estimate the hypocentroid. There are two strategies for this, which we term "direct" and "indirect" calibration. Direct calibration is based on using a carefully selected set of arrival time data to estimate the hypocentroid. In general, we restrict the data set to an epicentral distance range in which only direct crustal arrivals are observed, that is, before the Pg/Pn crossover distance. Direct *S* phases in this range are normally used as well. In Iran, the

Table 1. Velocity Model Used in the Relocation of Teleseismically and Regionally Recorded Events (1966–2013)[a]

Depth (km)	V_p (km s^{-1})	V_s (km s^{-1})
0–8	4.70	2.70
8–25	5.75	3.20
25–44	6.15	3.55
44–160	8.10	4.65

[a]The Moho depth is at 44 km, determined from Pn arrival times.

crossover distance is typically around 1.2–1.6°. Using the observed arrival time data, we can refine an average 1-D crustal velocity model (Table 1) that provides a good fit to the direct arrivals, and we can further reduce the biasing effect of unknown crustal velocities by further reducing the epicentral distance range, as long as azimuthal coverage is not sacrificed.

The second strategy, indirect calibration, takes advantage of other sources of constraint (i.e., other than seismic phase arrival times) on the location of one or more events in the cluster, such as observations of surface rupture, analysis of remote sensing observations such as InSAR, or independent locations of earthquakes from a temporary network (for which the arrival time data may or may not be available). When such constraints are available, the hypocentroid of the cluster can be calibrated by shifting the entire cluster in space and time to optimally match the available constraints. There are substantial complications, of course, in properly accounting for uncertainties when several constraints are available that may apply to different subsets of hypocentral parameters. See *Walker et al.* [2013a] for an example of this approach.

These two methods of location calibration are not mutually exclusive and if the data permit, both methods can be used and compared to gain further confidence in the resulting locations. We have done this with the Khaki sequence; however, we did not follow a strategy of basing our location calibration on the InSAR analysis presented in this study. The InSAR signal for such a relatively large event is so broad in extent that it would not be able to provide a good estimate of the hypocenter, and there is the question of resolving the focal plane ambiguity for buried events. However, there are sufficient other data to calibrate the cluster independently of the InSAR analysis, in both the direct and indirect manner, and that independence provides additional opportunities for understanding the seismotectonic implications of this interesting sequence, as well as providing additional confidence in the reliability of both the seismic and the remote sensing analyses.

3.1.2. Relocation of the Khaki Sequence

To improve the calibration of the Khaki sequence, we included events from the background seismicity of the region. Such events provide raypaths that improve resolution of the hypocentroid of the cluster through enhanced azimuthal coverage, and they provide a context in which it is easier to understand the significance of the 2013 sequence. The cluster includes an event as early as 1966, but most of the events occurred since about 1999. The 2013 sequence, including one foreshock, the main shock, and aftershocks through the end of the year, comprises 111 events out of the 176 in the cluster (the cluster size is limited by the permissible inversion size given the large number of free parameters with this many earthquakes). Of these, 17 events are in common with the month-long aftershock survey (section 3.2).

The arrival time data set for the Khaki sequence was assembled from the ISC Bulletin, the bulletins of the two main Iranian regional seismograph networks (operated by the University of Tehran Institute of Geophysics and the International Institute of Earthquake Engineering and Seismology, IIEES), recordings of the Iran Strong Motion Network (ISMN, operated by the Building and Housing Research Centre, BHRC), the bulletin of the Iraqi network, and data from the deployment of temporary seismic stations for aftershock monitoring of the Khaki sequence (section 3.2). Seismograms of the Iranian networks were in many cases repicked. Readings from the ISMN were converted to *S-P* times for relocation because those instruments do not have calibrated timing. We used arrival time readings for four of the larger aftershocks from the temporary seismic network deployed (section 3.2), and these data were of critical importance to calibrating this cluster.

The crustal velocity model that we developed for the Khaki sequence (Table 1), based on fitting the arrival times of direct-arriving and refracted *P* and *S* phases, is typical of those we have inferred for other clusters of earthquakes in Iran. This is done through forward modeling and differs from the velocity model found for the aftershock microseismicity (section 3.2) by only 0.15–0.5 km/s. Because a large amount of arrival time data was
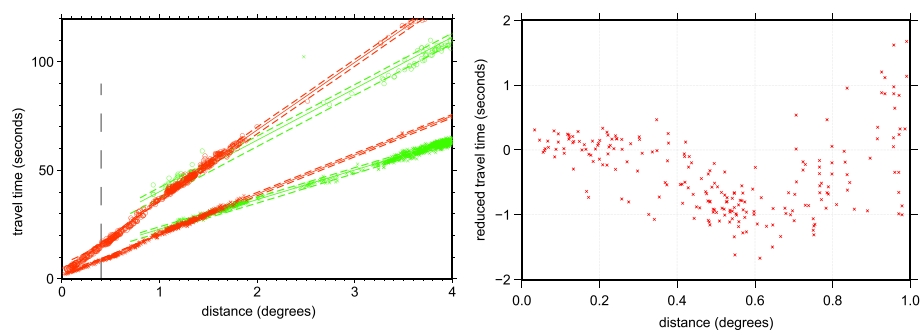
Figure 5. (left) Observed phase arrivals and traveltimes calculated from the local velocity model used for origin time calibration (section 3.1). Traveltime curves are shown for both *P* (Pg in red, Pn in green) and *S* (Sg in red, Sn in green) phases. *P* phases are indicated by a cross and *S* phases by circles. The dashed line indicates the epicentral distance range out to 0.4° used for calculating the hypocentroid. (right) Reduced traveltimes for Pg phase out to 1°. The reduction velocity used is 6.0 km/s.

available at close epicentral distances, we were able to resolve a three-layered crust that provides a reasonable fit to the observed arrival time data at distances out to the Pn/*P* crossover distance, around 17°. At greater distances we used the global model ak135 [*Kennett et al.*, 1995] to calculate theoretical traveltimes. With data at short range (within several focal depths of the epicenter) it is also possible to resolve the trade-off between focal depth and crustal velocities fairly well. Once focal depths are constrained by the fit to direct-arriving phases, the depth of the Moho interface in the model can be well constrained at 44 km by the Pn arrival times, in very close agreement with an estimate of ∼45 km from nearby receiver functions [*Paul et al.*, 2006]. Our estimates of regional upper crustal velocities are similar to those calculated from our month-long local aftershock deployment (section 3.2), as well as those determined from local earthquake recordings in the Ghir region of the central SFB, ∼100 km east of our study area [*Hatzfeld et al.*, 2003; *Tatar et al.*, 2004]. However, they are somewhat slower than those similarly determined in other parts of the Zagros [*Nissen et al.*, 2014, and references therein].

In the case of the Khaki sequence we observed an unusual complication in the arrival time data that forced us to restrict the epicentral distance range for the hypocentroid to only about 40 km. As can be seen in Figure 5 the observed traveltime versus distance plot features a concave downward (to shorter traveltimes) curve in the distance range from about 0.4 to 0.9°, in both the *P* and *S* arrivals. A one-dimensional velocity model with monotonically increasing velocities is unable to replicate such a pattern. Investigation showed that this pattern is mainly due to the arrivals observed at station AHBU located about 50 km northwest of the 2013 sequence. The spread of distances for the anomalous arrivals is due to the geographical scatter of the constituent events in the cluster. If we were forced to rely on these data for the calibration of the hypocentroid, it would be pulled as much as 5 km to the northwest. Fortunately, we had a strong data set of arrivals at shorter distances with good azimuthal coverage from the two deployments of temporary seismograph stations, which made it possible to isolate the problematic arrivals at AHBU. Most of the raypaths to AHBU lie nearly parallel to the prominent anticlines in this region, and we speculate that these are responsible for the distortion of observed arrival times. To avoid biasing the hypocentroid, we used only readings at less than 0.4° for that part of the location process, but this left us with 154 *P* and *S* readings with good azimuthal coverage.

In this distance range the data from the IIEES deployment are supplemented by *S-P* readings from accelerometer stations operated by BHRC, repicked, and also by arrival time readings from two other temporary seismic stations of the GSI deployment. Focal depths were held fixed because there are insufficient data to carry out a free-depth relocation for most events in the cluster (Table S1, supporting information). However, the depth of many events can be constrained by direct arrivals at near distances. Focal depths for the 2013 sequence are consistent with the free-depth solutions of the calibration events, ranging from about 7 to 14 km with an estimated uncertainty of about 3 km. Events for which no constraint was available were held at 10 km as this is near the median of depths that could be constrained from the data. The 2013 main shock hypocenter depth at which slip initiated is constrained by near-source arrivals at 11 km, again with an estimated uncertainty of about 3 km.
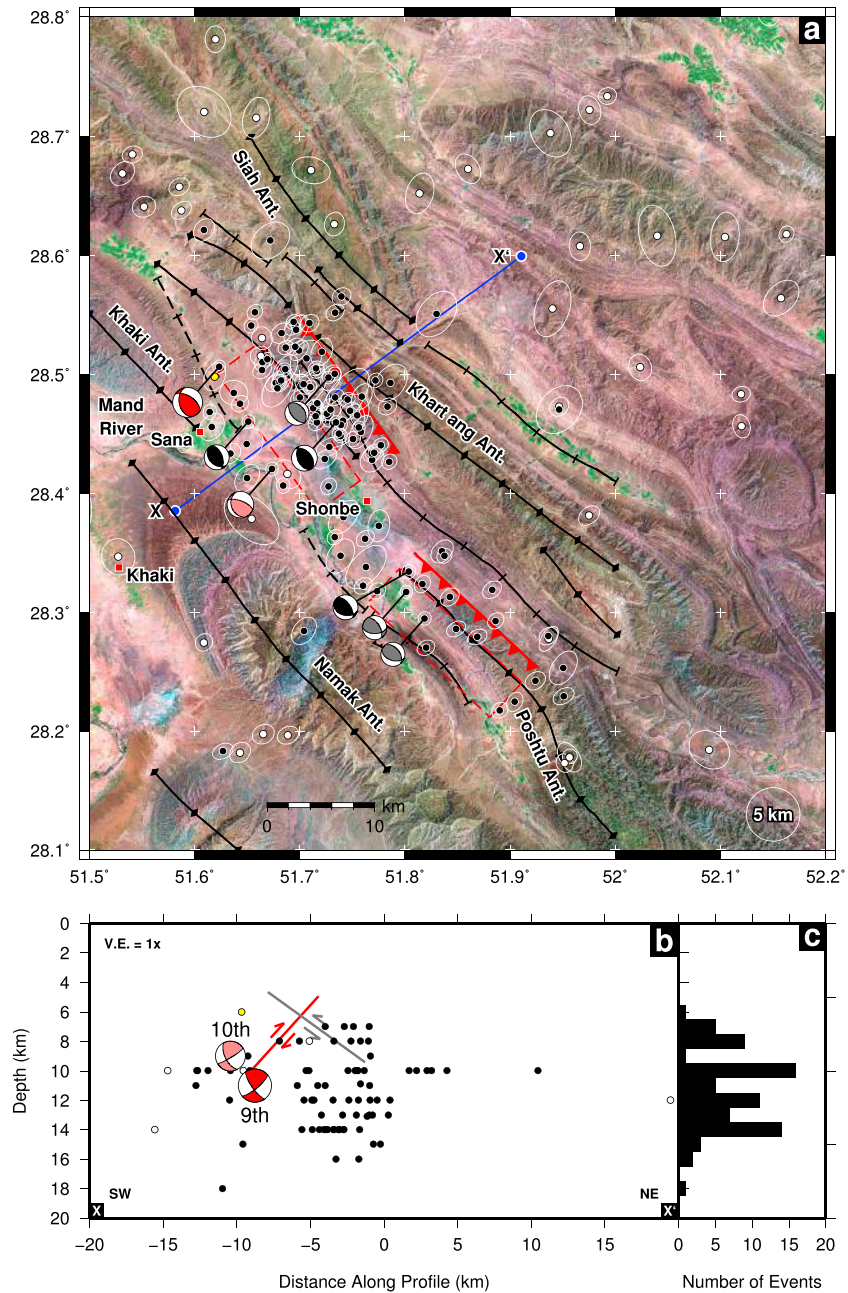
Figure 6. (a) LANDSAT image (RGB 742) of the epicentral region of the 9 April 2013 Khaki earthquake. The best fitting fault segments from the InSAR analysis and elastic dislocation modeling are shown as red lines (uniform slip patches as dashed outlines). Focal mechanisms (red and pink) from the body waveform analysis , and from the GCMT catalogue (black during the period of InSAR coverage, grey after) are offset slightly to the southwest from their relocated epicenters for the reasons of clarity only. Epicenters of smaller earthquakes are shown as circles (black circles are from after the Khaki earthquake, white before). The 55 hr M 3.9 foreshock to the main event is shown in yellow. All epicentral locations are those derived from HDC analysis and are displayed with their 90% confidence ellipses (white outline) for their relative location (see section 3.1 and Table S1, supporting information). (b) Cross section of earthquake relocations 8 km either side of the profile denoted X–X′ from southwest to northeast centered on the updip position of the main fault plane. Hypocenters of smaller earthquakes are shown as circles (black circles are from after the Khaki earthquake, white from before). Those hypocenters with fixed default depths at 10 km (denoted by a letter c in Table S1, supporting information) have been omitted. The selected SW dipping fault plane is shown in red and coincides with the relocation of the main shock hypocentroid. The NE dipping solution to the InSAR is shown in grey. (c) Histogram of earthquake aftershock depths along profile X–X′ for those earthquakes for which arrival phase information was available to constrain depth (black).

In part because of concern over the anomaly in traveltimes to AHBU discussed above, we calibrated the Khaki cluster using both direct and indirect methods. For indirect calibration the calibration events are four of the earthquakes for which the locally recorded data were available. For this purpose they were located separately as a four-event cluster, yielding free-depth solutions between 7 and 13 km and epicentral uncertainties of 800–900 m.

Relative to the direct calibration solution, the indirect calibration solution lies about 800 m to the ESE (azimuth 122°). This discrepancy is consistent with the uncertainty of the cluster hypocentroid calibration in the two methods: 1.1 km for indirect calibration and 1.9 km for direct calibration. In both these cases, nearly the same number of events (171 and 169, respectively) have final epicentral uncertainties of 5 km (90% confidence level) or better. One hundred fifty events in the cluster have epicentral uncertainty of 3 km or better. For the final reported locations (Table S1, supporting information and Figure 6) we have preferred the indirect calibration result, which we judge to be least effected by the evident heterogeneity in traveltimes in the region. The estimation of the hypocentroid is still subject to the effects of crustal heterogeneity because absolute traveltime residuals (not traveltime differences, as for the cluster vectors) are minimized for that estimation.

Thirteen of the 17 aftershocks that are common to the two aftershock data sets agree in their epicentral location within uncertainties. Comparison between the estimates of the depths for the two data sets shows that the difference between the estimates has a standard deviation of 2.3 km, with minimum and maximum differences of −5 km and 4 km, and with the focal depths for the calibrated events being on average almost 1 km deeper. Given the relatively small sample size, this may not reproduce the full extremes between the data sets.

The along-strike distribution in the densest concentration of aftershocks very closely matches the InSAR determined fault length for the NW segment of 16 km. The earthquake depths are mainly deeper than the InSAR-determined fault bottom depth of 10 km, with a smaller fraction occurring over the same depth interval as the slip (Figure 6c). This is in contrast to the more immediate locally recorded aftershocks in the month following the main shock which occurred over a wider depth interval including that of the imaged slip (4–10 km) and predominately above.

3.2. Locally Recorded Aftershock Microseismicity

The distribution of aftershocks in the month following the earthquake was determined using data recorded by a dense, local seismological network deployed around the epicentral area. This network consisted of 17 CMG-6TD, three-component seismometers connected to CMG-DM24 Guralp recorders, and was operated from 14 April until 16 May 2013, in the period 5 to 37 days after the earthquake. Details of the instruments and data processing techniques can be found in *Tatar et al.* [2005, 2007] and *Yaminifard et al.* [2012]. During the 5 week operation of the network, more than 1350 aftershocks were detected, ranging in magnitude from 1–5. These events were initially located using the Hypocenter 3.2 program [*Lienert and Havskov*, 1995], using a velocity model determined in an earlier microseismic experiment in the Central Zagros [*Hatzfeld et al.*, 2003; *Tatar et al.*, 2004].

We then selected a subset of 372 earthquakes with an azimuthal gap of ≤180°, an RMS residual (the difference between observed and calculated arrival times) of ≤ 0.3 s and at least 6 *P* and *S* phase readings with the aim of this event selection being to refine the velocity model. First, using the arrival times of this subset and applying the Wadati technique of the time separation of *P* and *S* arrivals, we calculated a V_p/V_s ratio equal to 1.84 (±0.04) for later use in determining the velocity structure. These selected events were then inverted using the VELEST program [*Kissling*, 1988], which simultaneously calculates improved hypocenters and a best fit, layered velocity structure. We used 50 randomly perturbed starting models to ensure convergence to the final structure [e.g., *Hatzfeld et al.*, 2003; *Tatar et al.*, 2005]. We kept only final models for which the 1-D inversion converges correctly (i.e., the rms decreases significantly to values less than 0.07 s). The details of determining the velocity structure are given in *Tatar et al.* [2005], but we provide a brief summary here: we start with a stack of 2 km layers of uniform velocity (6 km/s) and determine that no more than five layers are required in the inversion. The five-layer model was then randomly perturbed (with differences as large as 0.5 km/s in each layer) to obtain a set of initial models for the inversion. Again we used the uniform velocity of 6.0 km/s in our five-layer starting velocity structure. Our final velocity structure comprises five layers of V_p = 4.2 km/s (0–2 km), 5.2 km/s (2–4 km), 5.7 km/s (4–10 km), 5.9 km/s (10–14 km), and 6.1 km/s (below 14 km). We observe that the average rms for selected events decreased from 0.228 s to 0.097 s for our final velocity model, compared to the Central Zagros velocity structure *Hatzfeld et al.* [2003]. It is not clear which layer boundary corresponds to the cover-basement interface, but based on the results of other microearthquake monitoring in different
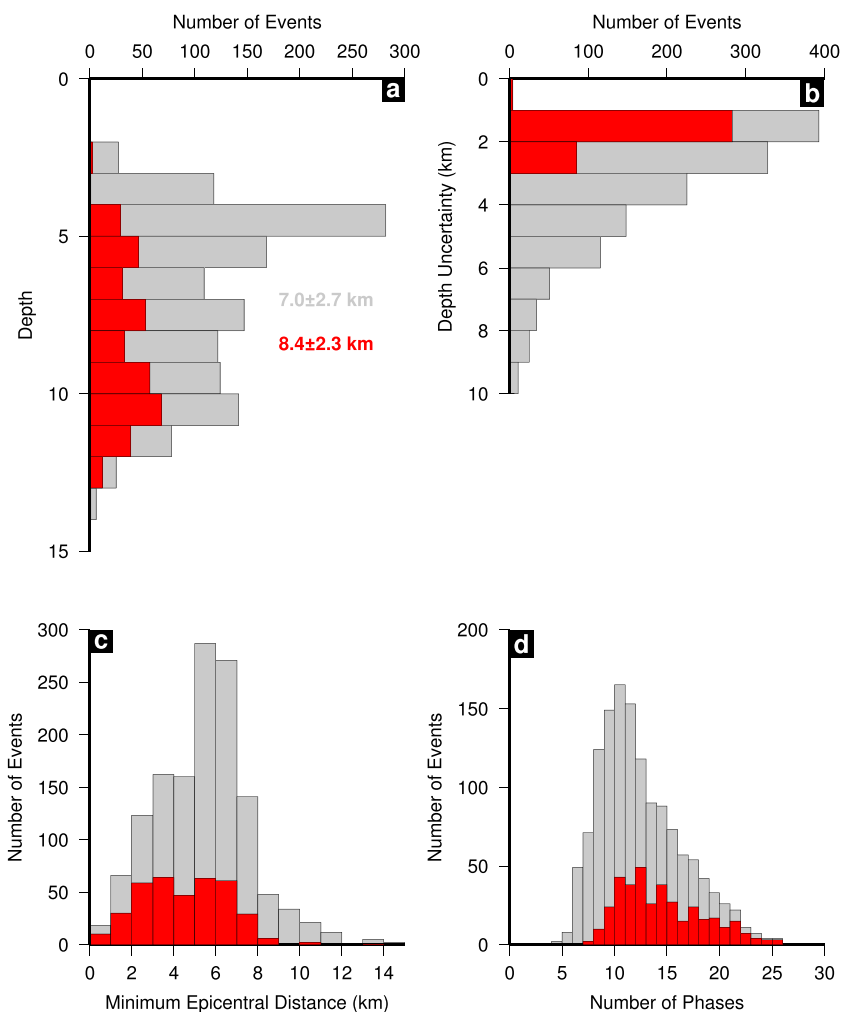
Figure 7. (a) Focal depths distribution of 1350 (grey) and 372 subset (red) locally recorded aftershocks. Numbers indicate the mean and standard deviation in depth for the two subsets. (b) Vertical uncertainties in aftershock focal depths. (c) Histogram of minimum epicentral distances between aftershocks locations and seismological stations. (d) Histogram of the number of phases (*P* and *S*) used for determining locations.

parts of Zagros [*Tatar et al.*, 2004; *Yamini-Fard et al.*, 2006; *Nissen et al.*, 2011], we estimate a minimum depth of ∼10 km for the basement where the *P* wave velocity reaches ∼5.9 km/s (although we cannot rule out a deeper basement at 14 km where there is another increment in velocity).

The full 1350 and selected subset of 372 aftershocks were located again using the updated velocity model and Hypocenter 3.2 program. The 372 selected events are more precisely located as they were selected based upon quality criteria of small azimuthal gaps and residual arrival times. While these criteria do not prevent any systematic bias, because our network closely surrounds the epicentral area, with an average minimum epicentral distance of ∼6 km (Figure 7), we are confident that such bias should be small. The accuracy of these locations horizontally and in depth is typically less than 2 km and 3 km respectively. With respect to the uncertainty in depth for the whole set of aftershocks (Figure 7b), about 30% have an uncertainty less than 2 km, and about 70% less than 4 km.

In an attempt to eliminate any relative scatter in locations due to local heterogeneity in the 1-D velocity structure, the earthquakes, which were previously located independently, were relocated using the double difference method HypoDD [*Waldhauser and Ellsworth*, 2000]. This method is particularly useful to map lineaments of earthquakes that may highlight discrete faulting. We choose to have source pairs with a minimum of 10 common observations (traveltimes to mutual stations) and distances between the paired events smaller than 6 km. As the seismicity is relatively tightly spaced, we are able to characterize the aftershock sequence as
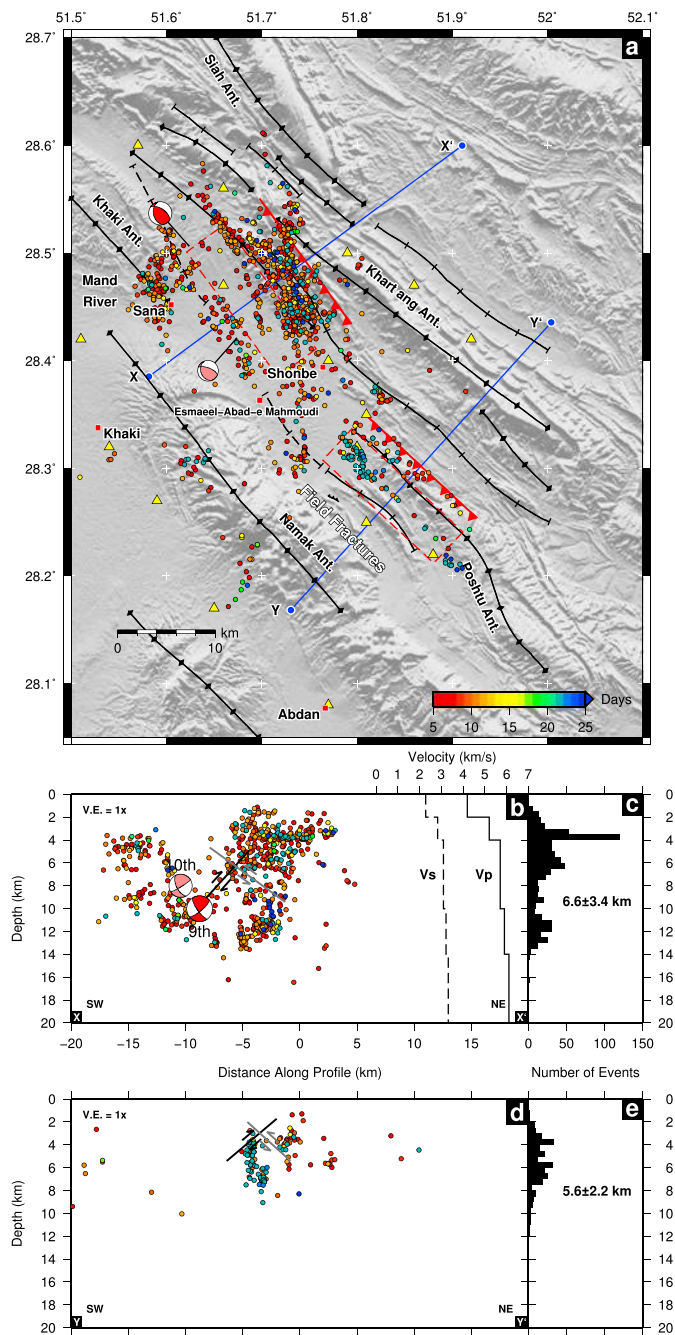
Figure 8. (a) Locally recorded aftershocks (1108) in the month following the earthquake (relocated with HypoDD), color coded by the number of days after main shock on the 9 April 2013. Locations of 15 of the local stations are denoted by yellow triangles. The SW dipping fault segments from the InSAR analysis and elastic dislocation modeling are shown as red lines (uniform slip patches as dashed outlines). Focal mechanisms (red and pink) from the body waveform analysis (Table 3), are shown just offset slightly from their teleseismically relocated epicenters (not covered by the locally recorded aftershock survey). Field observations of surface fractures in the locality of N28.2704°E51.778944°in the hanging wall of the SE segment are marked by a thin black barbed line. (b) Cross section of earthquake relocations 8 km either side of the profile denoted X–X' from southwest to northeast centered on the updip position of the main fault plane. The selected SW dipping fault plane is shown in black, with the NE dipping solution to the InSAR shown in grey. The black solid and dashed lines indicate the velocity-depth profile for V_p and V_s, respectively, determined in the relocation of the locally recorded aftershocks. (c) Histogram of earthquake aftershock depths along profile X–X'. (d) Cross section of earthquake relocations 8 km either side of the profile denoted Y–Y' from southwest to northeast centered on the updip position of the secondary fault plane. The selected SW dipping fault plane is shown in black, with the NE dipping solution to the InSAR shown in grey. (e) Histogram of earthquake aftershock depths along profile Y–Y'. The aftershock data are available in the supporting information.

a single cluster of 1108 events (Figure 8). The relative distribution of seismicity is better defined after relocating with the HypoDD technique, and it is these relocated epicenters that are shown in Figure 8.

There is a peak in the clustered seismicity depth distribution at 4–5 km, and a ~7 km long, NE trending, near-horizontal line is visible at this depth (Figures 8b and 8c). However, there may be some dependence upon the velocity model in the tight clustering of earthquakes at this depth as tests using very different velocity models (a 6 km/s half space or that from *Hatzfeld et al.* [2003]) reduces or eliminates the peak at this depth. The local recording of aftershocks commenced 5 days after the main shock, and most events occurred in the time period of 5 to 13 days but with some continued seismicity along the subhorizontal lineament and also a cluster of deeper events at ~10 km depth toward the end of the survey. The observed seismicity is not related to the activity of a major basement fault such as that thought to be responsible for the largest earthquake in the central Zagros, the M_s 6.9/M_w 6.7 Ghir earthquake of 9 April 1972 [*Berberian*, 1995].

For the southeastern fault segment, there are fewer aftershocks, and they are constrained over a shallower depth interval (2–8 km) (Figures 8d and 8e). However, a burst of events 22 days after the main shock occurred beneath the InSAR-imaged fault plane, in the depth range 4–8 km (this seismicity is outside the time period covered by the InSAR data). In map view, these appear to delineate a NNW-SSE trending structure, oblique to the principal structural trend in the area (Figure 8a). Between the two fault segments and also to the west of the northwestern segment, there are other clusters of seismicity that are NNW-SSE trending. These lineaments may represent minor dextral faulting related to the right-lateral shear in the region (Figure 4), as they are parallel to the Borazjan Fault, and in some cases are vertical or subvertical in extent.

3.3. Teleseismic Body Waveform Modeling

We have jointly inverted long-period *P* and SH waveforms to obtain the focal parameters of the Khaki main shock, and the largest aftershock in the sequence, which occurred a day later. We low-pass filter the seismograms in order to reproduce the response of a long-period (15–100 s) WWSSN instrument. We then invert for the focal parameters using Green's functions calculated for a point source, using the MT5 program of *Zwick et al.* [1994] (a version of the algorithm of *McCaffrey and Abers* [1988] and *McCaffrey et al.* [1991]). This procedure is commonly used, and thorough descriptions can be found in *Nabelek* [1984] and *Taymaz et al.* [1991]. We use stations with epicentral distances of 30–80° to avoid complications relating to core phases and shallow velocity structures. For our velocity model (Table 1), we use that calculated for the relocated aftershocks (section 3.1).

The best fitting solution for the main shock is shown in Figure 9. The length of the waveforms, which are a combination of the direct *P* and *S* waves, and their near-source surface reflections, provide constraints upon the depth. The body waveform analysis determines the equivalent point source of moment release at a centroid depth in contrast to the initiated point of rupture at the hypocentral depth. The misfit curves shown in Figure A1 demonstrate that the centroid depth (the slip-weighted average depth of moment release) is in the range 6–12 km, with a best fit at 9 km. The width of this range stems from the trade-off between the depth of the event and the length of the source time function, which also affects the length of the observed waveforms (and means that there is also a trade-off between moment and depth, Figure A1). Additionally, errors in the chosen velocity structure are not incorporated into this plot, so a further ±1 km range in the centroid depth is also possible. This places the centroid depth near the interface between the lower sedimentary cover and the top of the Hormuz salt based upon the velocity models and the structural cross section (Figure 3). The mechanism shows dominantly thrust motion on one of two planes striking roughly NW, with a small component of strike-slip motion.

The largest aftershock, one day after the main event (M_w 5.4), shows a very similar mechanism to the main shock (Figure A2). The epicentral relocation places the onset of the rupture in the middle of the NW fault segment, toward the bottom of the SW dipping InSAR determined slip plane (Figure 6), 10 km SE of the main shock hypocenter. Given the likely source dimensions of <5 km for an event of this size, this indicates that this aftershock did not contribute to the deformation seen on the SE segment.

The major difference between the main shock and largest aftershock body waveform solution is in their estimated centroid depth, which at 2–7 km for the aftershock (with a best fit of 5 km) is shallower than that estimated for the main shock (9 km). This therefore places the aftershock entirely within the sedimentary cover.
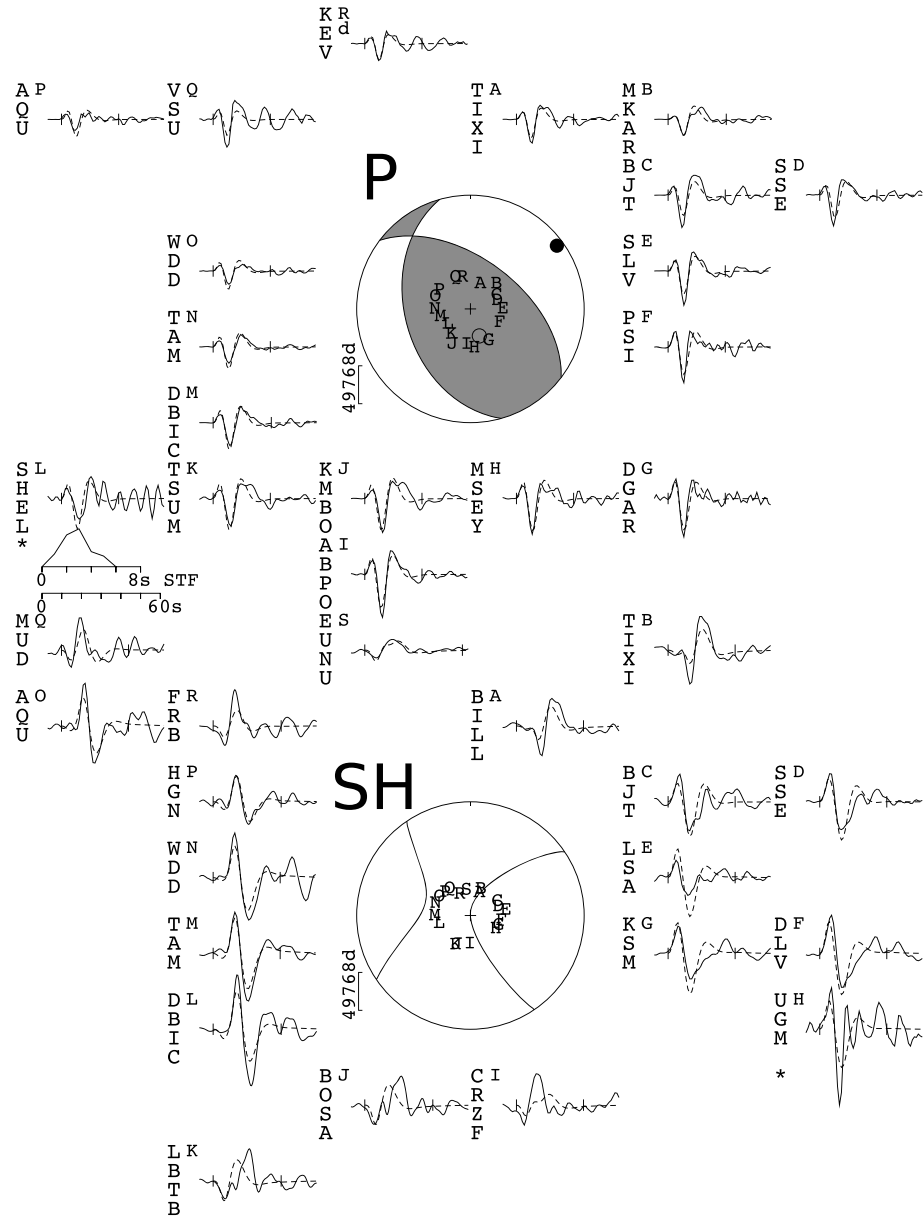
Figure 9. Mechanism of the Khaki main shock, from the inversion of *P* and SH body waves. The event header shows the strike, dip, rake, centroid depth, and scalar seismic moment (in Nm) of the minimum misfit solution. The top focal sphere shows the lower hemisphere stereographic projection of the *P* waveform nodal planes and the positions of the seismic stations used in the modeling routine. The lower focal sphere shows the SH nodal planes. Capital letters next to the station codes correspond to the position on the focal sphere. These are ordered clockwise by azimuth, starting at north. The solid lines are the observed waveforms, and the dashed lines are the synthetics. The inversion window is marked by vertical lines on each waveform. The source time function (STF) is shown, along with the timescale for the waveforms. The amplitude scales for the waveforms are shown below each focal sphere. The *P* and *T* axes within the *P* waveform focal sphere are shown by a solid and an open circle, respectively. Stars mark seismograms not used in the inversions due to large amounts of noise or anomalous amplitudes compared to nearby stations.

Table 2. Zones of Fissuring and Surface Cracking Observed After the Khaki Earthquake to the Southeast of Shonbe[a]

Latitude	Longitude	Notes
51.8848	28.2356	rockfall and small landslide close to drainage
51.8878	28.2233	stone (~10 cm) saltation 1–12 cm
51.7891	28.368	rock fall
51.8302	28.3302	rock fall
51.8011	28.3606	rock fall
51.8358	28.3367	rock fall
51.8584	28.2439	quicksand at the river beach
51.8552	28.2449	rock fall
51.091	28.3499	Darvishi village; strong ground shaking
51.7757	28.272	surface fracture; bed geometry: N63W, 70NE
51.8043	28.2611	conjugate faults in rock outcrops; no clear trace of triggered slip
51.8074	28.2497	Keredeleh village; weak ground shaking
51.7785	28.2706	surface fracture; parallel the outcrop surface; bed geometry: N63W, 70NE
51.7812	28.2692	surface fracture; parallel the outcrop surface; bed geometry: N63W, 70NE
51.7698	28.2744	surface fracture; parallel the outcrop surface; bed geometry: N55–65W
51.7858	28.2691	liquefaction
51.8643	28.1943	Quaternary fault/fractures: N20W, 32NE; Dip of the young beds: N18W, 67NE
51.7848	28.3544	surface cracks and fissures
51.6977	28.3633	Esmaeel-Abad-e Mahmoudi; surface cracks and fissures
51.7633	28.3925	Shonbe; strong ground shaking
51.6473	28.4331	liquefaction

[a]The field observations are recorded from a survey to the area in the period 2–3 weeks following the earthquake.

4. Field Observations and Satellite Imagery

Field surveys were conducted during the period 2–3 weeks after the earthquake in order to map the extent of ground surface effects associated with the earthquake, such as mass movements (landslides and rockfalls), fissuring/cracking, and liquefaction resulting from strong shaking, as well as to look for any evidence of surface rupture. Surveying of such ground displacements and refining the record of seismicity (e.g., possible surface faulting, fracturing, and liquefaction) is an important goal for hazard forecasting and risk mitigation in this part of the Zagros. The severity of ground shaking through the earthquake area (assessed from surveying the effects on the ground surface and through questionnaires) decreases irregularly with distance from the epicenter, and we found a rapid decrease in the earthquake ground effects to the north and northwest of the main shock, as might be expected for a unilateral rupture that propagated southeastwards (section 3.1). However, the impacts of coseismic shaking are considerable between the Mand river valley and the NE flank of the Namak anticline (20 km SE of the epicenter and 5 km SW of Shonbe, Figure 8), and a maximum epicentral intensity of VIII on the Modified Mercalli Intensity (MMI) scale has been assigned at the village of Shonbe. Field observations and Google Earth satellite imagery showed that the village of Shonbe has a low liquefaction susceptibility because of its location at the edge of a fan which would drain groundwater toward the valley of the Mand River, and the severe damage to this village is largely the result of direct shaking rather than liquefaction. Toward the southeast of the village of Shonbe, the thickness of Quaternary deposits decreases and mean land slope increases. Further downstream, the Mand river drains across the general trend of the Zagros fold structures, and the elevation of the terraces with respect to the active channel drops to close to zero, indicating more subdued incision further southwest of the main shock.

There were several clear examples of liquefaction caused by temporary loss of soil strength during shaking, mostly along the Mand River (e.g., 51.7858°E, 28.269°N). Most examples of liquefaction we visited occurred within cultivated areas (Figure 1d), where the liquefaction susceptibility is high. The damage in the settlement of Esmaeel-Abad-e Mahmoudi (51.6978°E, 28.3633°N, Figure 1) resulted in part from this susceptibility. In general, evidence of liquefaction and fissuring up to 30 cm wide occurred over a total area ~400 m² in this immediate region.
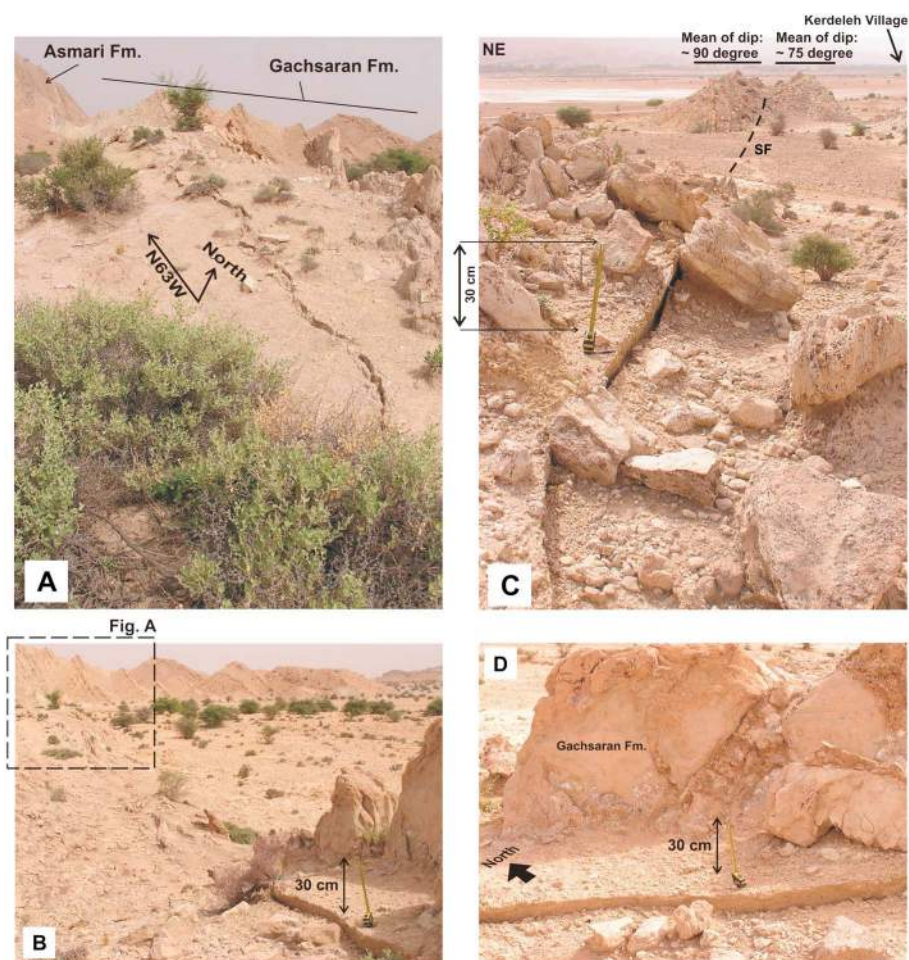
Figure 10. (a) Photograph looking northwest along surface fractures (N28.2704°, E51.778944°; N63W). This location is 10 km south of Shonbe, in the hanging wall of the southeastern fault segment. The surface fractures can be traced in a NW-SE direction for 4–5 km (Figure 8). The SW facing fracture at this location is approximately 0.11 m high along a near-vertical to steeply dipping plane (70±4°NE) developed in middle portion of the Gachsaran Formation (Miocene evaporites), parallel to the bedding. (b) Photograph looking northwest again along trace of the surface fracture; note: tape measure in the bottom right corner for scale. (c) looking east-northeast along the surface fracture; note the change in dip of the different layers on both sides of the trace of the surface fracture by about 15°; SF marks a small west facing fold observed where the fracture traverses the floodplain; here the height of the SW facing fracture is limited to ~2–3 cm, (d) near-vertical SW facing fracture developed in evaporates layers of the Gachsaran Formation.

There are no previously mapped landslides within the earthquake area. Following the earthquake, some small landslides were observed in the epicentral area, ESE of the main shock (e.g., 51.8848°E, 28.2356°N). Several rock-falls were also triggered by the earthquake, including a concentration within the core of the Namak anticline. We observed six sites with multiple rockfalls (Table 2) with a maximum volume of ~80 m^3. Further ground subsidence occurred between the northeast flank of the Namak and the Mand river valley (51.7085°E, 28.3734°N).

From the field work we found no evidence in the surface geology which indicates that the earthquake rupture broke through to the surface, in common with all previously studied earthquakes in the SFB. However, we did observe a NW-SE trending zone of en-echelon cracks and fractures, 9 km SE of the main shock (Figure 10), which we suspect were generated during or immediately after the earthquake (see also *Nissen et al.* [2007a], in which similar features were observed after the 2005 Qeshm earthquake, which were considered related to bedding plane slip within the hanging wall of the fault). The total length of the fracture zone is about 4–5 km, and its width ranges from 30 cm to a few meters (Figure 8). In the central portion of the fractures zone (Figure 10, Table 2; 51.7812°E, 28.2692°N) we found a single fracture with ~11 cm maximum vertical displacement (up to the NE).
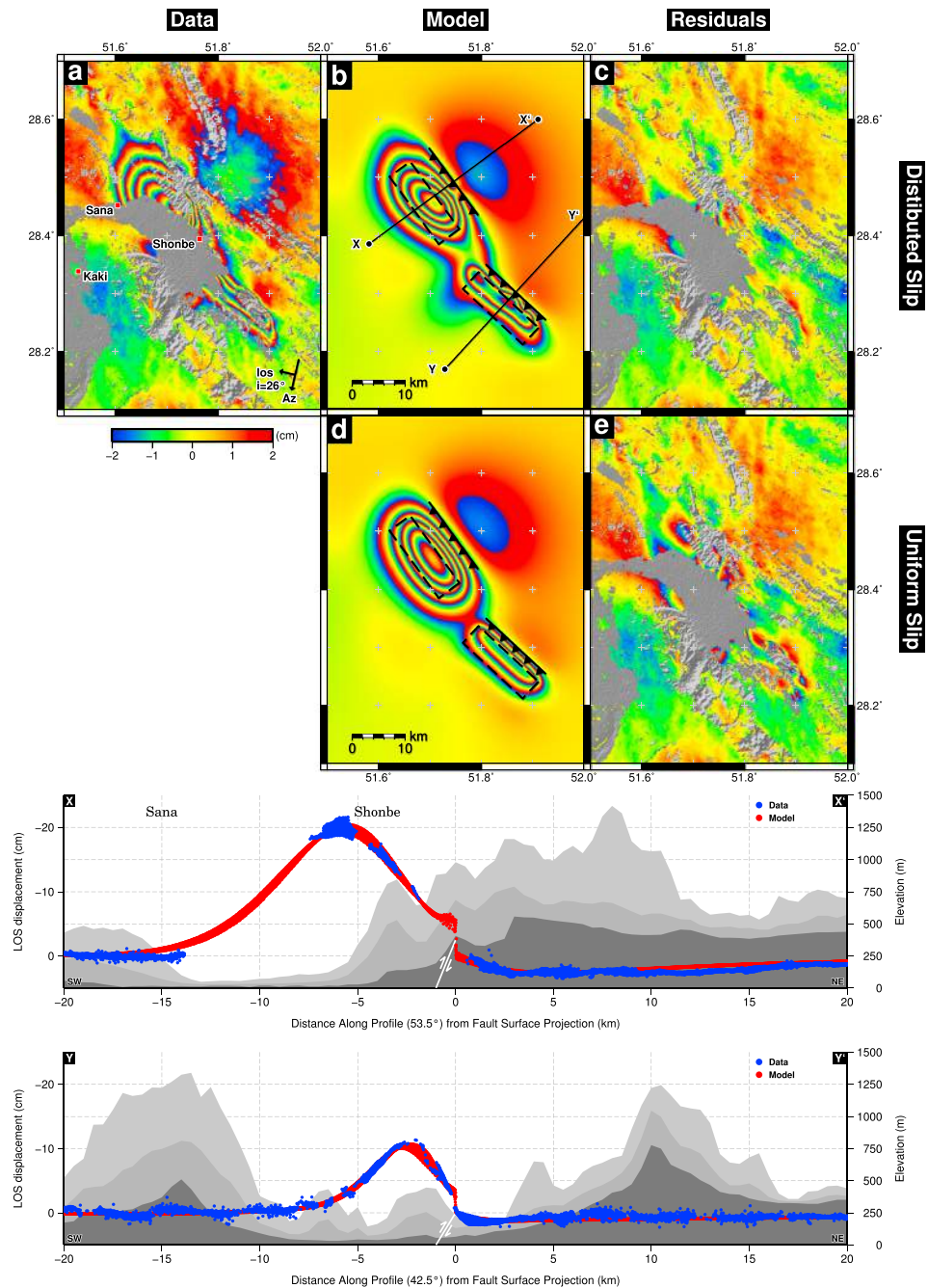
Figure 11. Interferogram, models, and residuals based upon distributed and uniform slip modeling for the Khaki earthquake. Colors show range changes as fringes rewrapped to 4 cm, with color cycles blue through yellow to red indicating motion away from the satellite. The updip projection of the fault segments are marked by the pair of barbed solid lines (triangles on the hanging wall), the surface outline of the uniform slip regions by dashed rectangles. The satellite track azimuths (Az) and line-of-sight directions (LOS) with angle of incidence (i) are indicated by black arrows. Profile X–X' through the RADARSAT-2 data, model, and topography is shown at the bottom. The profile is taken perpendicular to the strike of the fault segments. InSAR displacements are represented by blue dots, the modeled data projected into the same line of sight by red dots. Profiles of topography are taken from the SRTM 3 second data along the same sections, sampling 10 km wide swaths and showing minimum (dark grey), mean (grey), and maximum (light grey) elevations. The line-of-sight displacement axis has been inverted so negative motion (which is toward the satellite and mainly uplift in this case), is to the top of the figure.

5. Fault Geometry and Slip Distribution as Determined by InSAR

We provide additional constraints on the location and geometry of faulting using ground displacements recorded in a pair of RADARSAT-2 C-band SAR images. A descending interferogram (with a center angle of incidence of 23°) covering the coseismic period was created from SAR acquisitions on 12 October 2012 and 24 April 2013 (interferometric methods are described in Appendix B). Therefore, the interferogram (Figure 1) encompasses the period of the main shock on 9 April 2013, the largest aftershock the day after (M_w 5.4) and also 14 days of any postseismic deformation which included three further M_w 5.0–5.2 reverse faulting earthquakes recorded in the GCMT catalogue (Figure 6), as well as any potential premain shock signal.

The interferogram covers most of the near and all of the far-field deformation and captures a peak displacement of 25 cm toward the satellite and up to 5 cm of subsidence in the northeast. Coherence is lost in the Mand River valley, most likely due to agricultural and fluvial processes changing the nature of the ground surface over the five and a half month period of the interferogram. The displacement field has two main loci of deformation, the larger of the two focused at 51.71°E, 28.45° and the second 15–20 km to the SE at 51.88°, 28.24° (>10 cm). Both have closed fringe patterns with an asymmetry in the gradient of deformation, with more closely spaced fringes on the northeast side of the peak displacement than on the southwest side. The deformation field also exhibits a transition from ground motion toward, and then away from, the satellite moving from the peak displacement in the valley toward the hills NE of the Khart and anticline. These initial observations support reverse slip on two buried fault segments.

We use elastic dislocation modeling [*Okada*, 1985; *Wright et al.*, 1999] to determine a more precise fault geometry from the ground displacements and to try to resolve the focal plane ambiguity for this event. The main methods of forming the interferogram, downsampling of data, and the modeling approach are described in Appendix B. The use of InSAR surface deformation measurements does not necessarily permit the determination of the actual rupture plane when fault slip does not break the surface, and there is a lack of a clear discontinuity in the InSAR displacement field. This is particularly the case for earthquake burial depths that are large relative to the vertical fault dimensions [*Nissen et al.*, 2010; *Elliott et al.*, 2011], as well as in cases where the available InSAR observations are limited to a single-look direction, in which case other information is required to resolve the ambiguity. Furthermore, for buried sources, a trade-off between the fault slip and the fault width occurs so that the misfit to the data decreases (albeit marginally) as the slip increases and the fault narrows to a line source. Therefore, we test the fit to the deformation field for both NE and SW dipping fault planes. For the NW fault segment, solving for the fault geometry for both a NE and SW dipping plane with slip as a free parameter does result in the geometry collapsing to a line source, and the solutions for the opposing dip directions converge to approximately the same position in space. We therefore perform the inversion with slip fixed in intervals to assess the significance of changes in the calculated misfit as the prescribed slip increases (Figure B1). The misfit for both dipping planes decreases rapidly as the slip is increased from 0.1 to 0.8 m. For values above ~0.8 m of slip, the misfit does not significantly improve, but the slip-to-width ratios become rapidly large relative to that expected from known distributions of earthquake scales [*Wells and Coppersmith*, 1994] and increasingly physically unreasonable. Therefore, we select 0.8 m for the value of slip. Additionally, the difference in misfit to the InSAR data (Figure B1) is almost indistinguishable between the NE and SW dipping solutions (compare Figure 11 with Figure B2), so we are unable to determine the focal plane ambiguity with InSAR alone. However, only the SW dipping fault plane is consistent with the hypocentral relocation analysis for the main shock (section 3.1), as this fault plane intersects the hypocenter at its minimum misfit depth of ~11 km (Figure 6). For the NE dipping fault plane to be correct, this would require a much shallower hypocenter depth of ~4 km, well outside of the uncertainties of our solution (11 ± 3 km). In turn this would imply downdip rupture from the shallowest portion of the fault, which seems less plausible. Therefore, we use only the SW dipping fault plane for the rest of the analysis.

Conversely, for the SE segment, we are able to resolve the focal plane ambiguity based upon the InSAR modeling alone, as the slip on this plane is shallower and the data coverage around this segment is more complete. For this SE segment, there are slightly larger residuals on the NE side of this segment for the NE dipping fault plane compared to the SW dipping solution. Additionally, the required line-of-sight displacements on the south and southwest side of the main lobe of deformation are the wrong polarity compared to the data for the case of the NE dipping fault plane (which requires motion away from the satellite, when the data indicate motion toward). We therefore select the SW dipping solution (Table 3) for this fault segment. This segment

Table 3. Fault Parameters for the Khaki-Shonbe Main Shock and Aftershock Derived From InSAR Phase Measurements (Main Shock Only), Teleseismic Body Waveform Modeling and the Best Double-Couple Solutions in the Seismic Catalogues From the GCMT [Ekström et al., 2005; Dziewonski and Woodhouse, 1983] and the USGS-NEIC Body Wave [Sipkin, 1982] and W Phase Moment Tensor [Hayes et al., 2009; Kanamori and Rivera, 2008][a]

Solution	Strike (°)	Dip (°)	Rake (°)	Slip (m)	Longitude (°)	Latitude (°)	Length (km)	Width (km)	Top Depth (km)	Bottom Depth (km)	Centroid Depth (km)	Stress Drop (MPa)	Moment 10^{18} (Nm)	Magnitude M_w	Slip Vector (°)	P Axis Azimuth (°)
Khaki 9 April 2013 M_w 6.2 Main Shock, 11:53 UTC																
InSAR-NW	144	48	95	0.80	51.746	28.493	15.9	7.2	4.9	10.3	7.6	2.1	2.0	6.1	47	51
1σ	±1	±2	±4	fixed	fixed	fixed	±0.7	±0.4	±0.2	±0.5	±0.3	±0.1	±0.1			
InSAR-SE	132	40	107	0.25	51.867	28.302	15.6	5.8	1.7	5.4	3.6	0.8	0.5	5.7	20	30
1σ	±1	±4	±10	±0.03	fixed	fixed	±0.6	±1.0	±0.2	±0.7	±0.4	±0.2	±0.1			
InSAR Fix λ	144/132	48/40	95/107											6.2		
BW (this study)	164	42	119		51.623	28.507					9		2.0	6.1	35	54
USGS-BW	182	59	154		51.620	28.509					14		2.7	6.2	16	52
USGS-WCMT	147	20	103		51.249	28.399					11		5.5	6.4	43	47
GCMT	157	41	117		51.62	28.27					12		3.5	6.3	33	48
Khaki 10 April 2013 M_w 5.4 Aftershock, 01:58 UTC																
BW (this study)	158	32	133		51.673	28.421					5		0.14	5.4	21	38
USGS-BW	169	38	151		51.631	28.434					6		0.17	5.4	13	38
USGS-WCMT	138	40	116		51.493	28.350					15		0.16	5.4	16	30
GCMT	159	39	133		51.65	28.24					12		0.2	5.5	19	39

[a]The latitude/longitude locations for the faults are the centroid for GCMT, the epicenters for the USGS-NEIC Body Wave solution (USGS-BW), and USGS-NEIC W-Phase moment solution (USGS-WCMT), and the relocated epicenter calculated here (BW-this study) and the center of the updip projections of the fault segment to the surface for the InSAR solutions. The apparent average static stress drop (Δσ) is calculated from the segment moment M_0, width W and length L using the relation $\Delta\sigma = 8M_0/(3\pi W^2 L)$ [Scholz, 2002].

does not have a strong slip versus width trade-off that results in it not collapsing to a line source as for the NW segment, so we are able to also solve for the slip on this segment.

The main segment in the northwest consists of a SE-striking fault with near pure reverse slip on a 48°SW dipping plane with an equivalent centroid depth of 7.6 km. The southeasterly segment also strikes to the southeast with a similar dip of 41° and involves reverse slip with a greater degree of right-lateral motion. However, due to only having a single-look direction in the interferogram data, the angle of rake is poorly constrained for both these fault segments (Table 3 and Figure B3). The strikes and dips of both segments are however, better constrained, as are the segment lengths and depth extents. The two segments have the same fault length (16 km) and similar downdip widths (6–7 km), indicating a rather elongate rupture pattern that is over 30 km in length over the two segments, while relatively narrow its depth extent. Additionally, the SE segment is 4 km shallower than the NW segment at an equivalent centroid depth of 3.7 km, indicating a change in the depth range of fault slip. Neither segment is modeled as requiring significant slip to reach to the surface in order to fit the InSAR data (as is shown by the closed pattern of the InSAR fringes at the transition from the hanging wall to the footwall), but decorrelation, especially around the updip surface projections of our model faults, means we can not rule out minor decimetric surface slip in some areas. The fit to the interferogram data using the uniform slip patches for the two fault segments is shown in Figure 11. There is a ∼5 km right-stepping offset between the two segments and the village of Shonbe sits within this step over, where the highest MMI values were recorded. The uniform slip on this secondary rupture is about 25 cm, and the moment is 0.5×10^{18} Nm (assuming Lamé elastic parameters of the half-space equal to $\lambda = \mu = 2.2 \times 10^{10}$ Pa), which is equivalent to a moment magnitude of M_w 5.7. The M_w 5.4 aftershock that occurred 14 h after the main shock is not associated with the slip seen on this segment as the calibrated earthquake relocations place the M_w 5.4 aftershock 8 km to the NW in the center of the hanging wall of the NW segment (Figure 6). The updip surface projection of the northwestern fault segment lies 15–20 km east of the Khaki anticline and 20 km NE of the Namak anticline. The southeastern segment projects to the surface to the NE of the Poshtu anticline.

Comparing the InSAR fault plane of the main (northwestern) segment with the body waveform solution (Table 3), we find a similar dip but a discrepancy in the strike of 20°. The InSAR strike is very tightly bound by the elongation direction of the interferogram fringe patterns, which also matches the strike of the local anticline axes (Figure 6). The strike of the body waveform solution can be made to match with that from the InSAR for only a relatively modest misfit increase to the seismograms. This is due to the combination of the slightly oblique thrusting mechanism and the poor signal-to-noise ratio of seismograms on ocean islands, which means there is poor station coverage for the only (SH) nodal plane to cross near the center of the focal sphere (where teleseismic data has its maximum sensitivity). The InSAR fault center depth for the northwest segment (7.6 km) agrees to well within the ∼4 km accuracy of the seismological estimate of 9 km. The moment for the body waveform solution is 80% of the combined two fault InSAR solution but has the same moment as for the the NW segment (Table 3). Including the moment contribution from the M_w 5.4 aftershock that was also captured by the InSAR displacement field reduces this discrepancy slightly. While such a discrepancy appears to be quite common for earthquakes in the Zagros [e.g., *Nissen et al.*, 2010], the total InSAR moment is larger and the RADARSAT-2 data used encompasses a time period of 2 weeks after the main shock. Therefore, it is possible that there is a significant component of postseismic motion contributing to the mapped distribution of slip in the form of aseismic slip, such as shallow creep, as was observed following the 1994 Sefidabeh earthquakes in eastern Iran [*Copley and Reynolds*, 2014]. Attributing the deformation related to the SE segment as likely due to aseismic slip in the 2 week period after the main shock would resolve much of this moment discrepancy. However, part of the moment discrepancy could also arise from the use of the layered seismic velocity model versus an elastic half-space in the InSAR analysis, although we select a rigidity modulus of 2.2×10^{10} Pa for the half-space to approximate that used in the body waveform analysis in order to make the moments more comparable.

5.1. InSAR-Derived Slip Distribution

To further investigate the distribution of slip along strike and at depth for the Khaki earthquake, we expand upon the uniform slip modeling of the previous section by breaking the two known reverse fault segments up into 1 km patches and solving for variable slip (*Funning et al.*, 2005; *Elliott et al.*, 2012, see Appendix B for methods). We also examine the extent to which we are able to resolve the pattern of slip at depth and the sharpness of slip gradients.
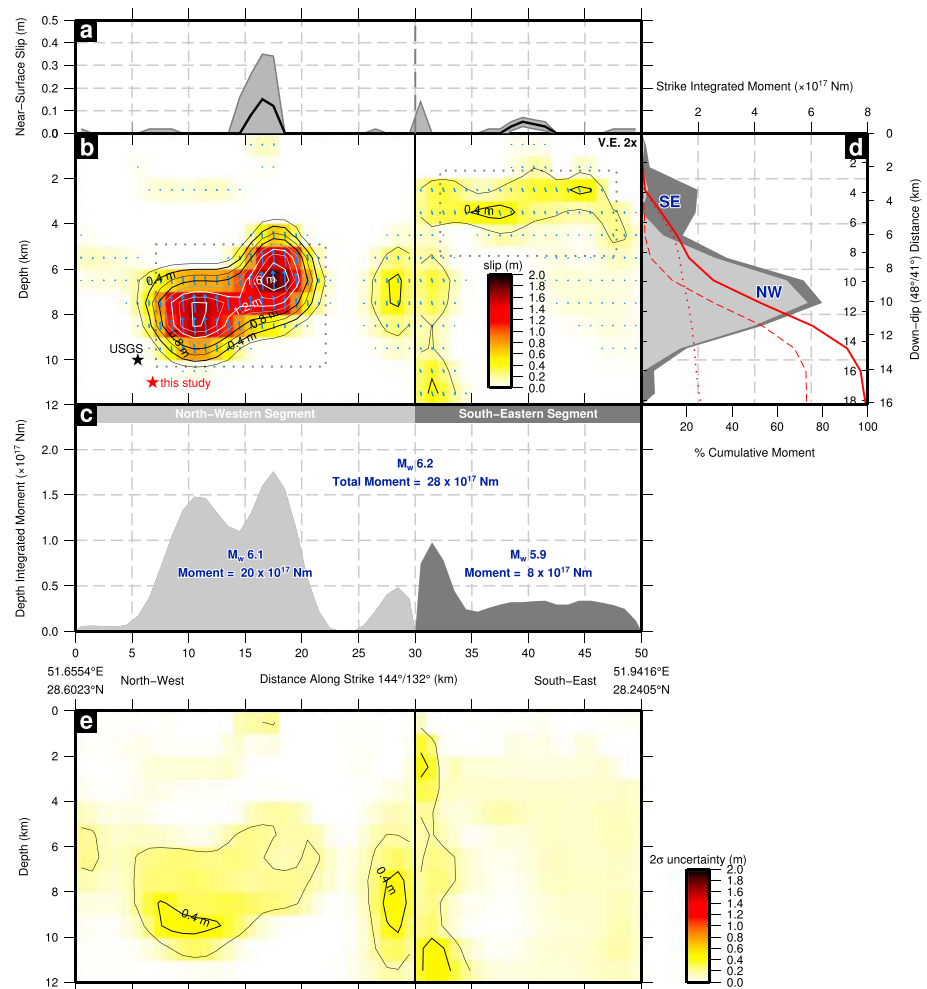
Figure 12. (a) Predicted surface offsets (black) with 2 sigma uncertainty bounds (grey) based upon the top 1 km cell in the InSAR distributed slip model. (b) InSAR-derived slip distribution with 20 cm contours. Blue slip vectors indicate the motion of the the hanging wall relative to the footwall. The red star is the relocated epicenter from this study. The black star is the strike perpendicular projection of the USGS hypocenter onto the fault plane at a depth of 10 km. The dashed grey box indicates the uniform slip plane extents. (c) Along strike integrated moment in each 1 km depth interval. (d) Depth integrated moment along strike of the fault at 1 km intervals. The total cumulative moment with depth is denoted by the thick red line (the dashed line is the contribution to the moment from the northwestern segment, the dotted from the southeastern segment). (e) Two-sigma uncertainty in distributed slip calculated from the standard deviation of 100 perturbed interferogram data sets based upon the atmospheric noise in each individual interferogram. Slip and uncertainty values for both segments are available in the supporting information.

The fit to the data for the distributed slip model is shown in Figure 11. There is a decrease in the residual fringes in the near-field with a improvement in the RMS misfit to the downsampled data from 0.87 cm to 0.64 cm (the far-field noise in the downsampled interferogram is ∼0.3 cm) and a reduction in the peak residuals from ±5 cm to $^{+2}_{-4}$ cm (Figure B4), in moving from a uniform to a distributed slip model.

The distribution of slip is shown in Figure 12. The northwestern segment has an estimated peak slip of 1.8 m at 6 km depth, with a likely resolvable pair of 5 km wide slip asperities seen in the pattern of contoured slip (based upon resolution tests, Figure B5). The western half of this segment has slip abruptly ceasing at 6 km depth, while the eastern second lobe has slip that continues to a shallower depth of ∼4 km. The depth extent over which significant slip (above the estimated uncertainty from the Monte Carlo analysis, Figure 12e) is modeled to have occurred for this segment is 5–10 km, matching well the extent of the uniform slip model. The southeastern segment has a tightly constrained slip distribution between 2 and 4 km (Figure 13), around half of the vertical extent of the uniform model. Modeled slip at the ends of the two fault planes has a high
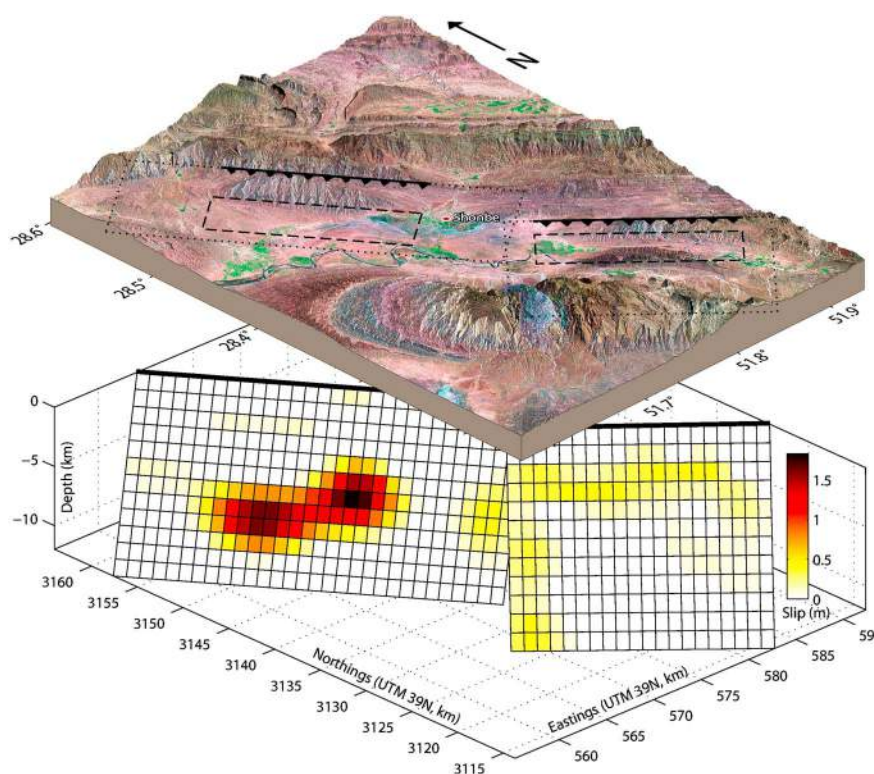
Figure 13. (top) Perspective Landsat (742) view of the earthquake epicenter with the updip fault projections marked by black arrows, either side of the town of Shonbe. The dashed boxes mark the outline of the slip at depth from the uniform slip model and the dotted boxes that of the distributed slip model. (bottom) Distribution of slip based upon the InSAR modeling. Significant slip (0.1 m+) occurs over the depth range 5–10 km for the main northwestern segment, and 2–4 km for the southeastern segment.

level of uncertainty (Figure 12e) due to the lack of InSAR coherence above the faults planes in this region and is therefore likely spurious noise.

The slip distribution and profiles of modeled displacement (Figures 11 and 12) point to at most decimetric slip at the surface that is not resolvable within the uncertainty of the model. This predicted small (potentially zero within uncertainty of the model) surface offset is consistent with the lack of primary surface ruptures observed in the field.

6. Discussion

From the analysis presented earlier on the earthquake, local seismicity, and slip, we are able to make inferences on the spatial relationship between the instantaneous uplift and the longer-term geological structures, as well as the possibility of triggering of aseismic slip on adjacent fault segments and the potential role of lithology in determining the depth segmentation of slip.

From the uniform slip model, we can calculate the instantaneous vertical component of surface displacement due to this earthquake (Figure 14). The modeled maximum uplift is just over 20 cm. The highest point of the anticline rises 800 m above the local base level. The coseismic uplift does not match the location of the surface anticlines. The peak of the uplift is shifted 3 km southwest of the peak in this topography and the fold axial surface trace (Figure 14), but the along-strike extent of the uplift pattern seems more similar to the length of the surface expression of the anticline. Modeling the expected uplift pattern from the same magnitude of slip but over the shallower depth range of 2–5 km and then adding this to the uplift measured in this earthquake, we see that the uplift is now more centered on the anticline trace, although with a greater asymmetry than seen in the anticline and still a larger width (Figure 15d). This may indicate that in the longer-term shallower slip occurs (either aseismically in the postseismic period or seismically in further earthquakes). One potential
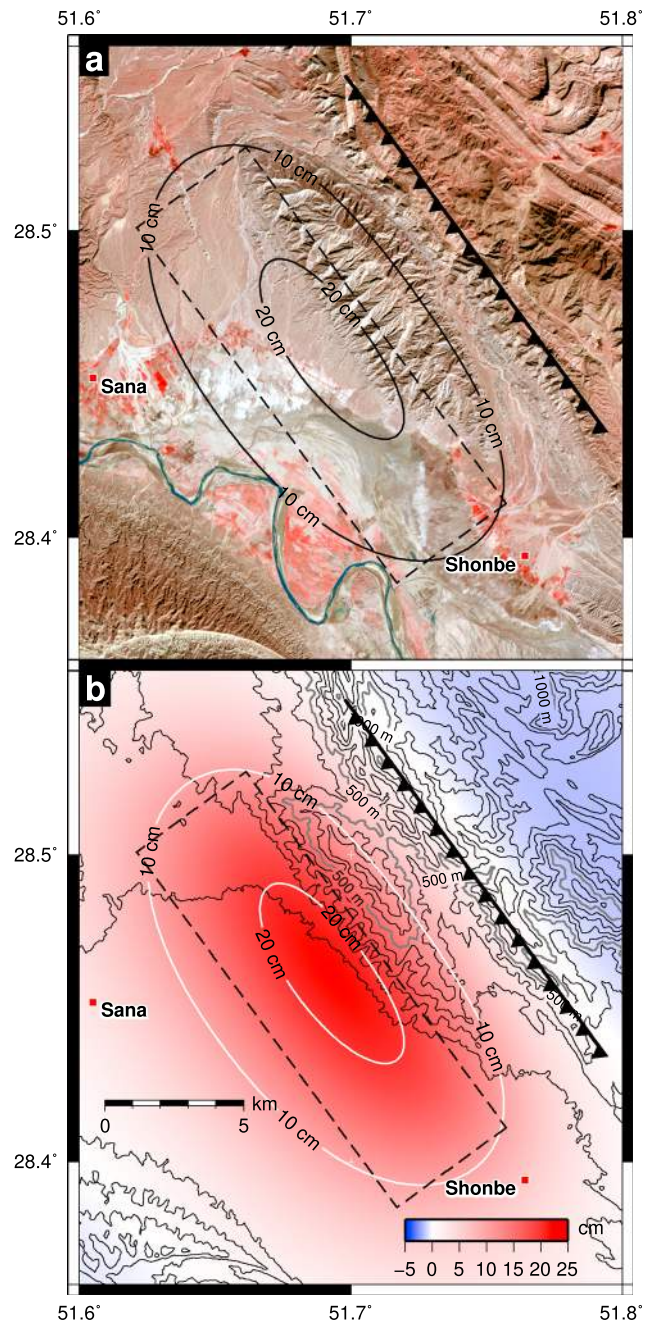
Figure 14. (a) ASTER image (RGB 321) of the NW segment (red line), showing the anticline north of Shonbe. Ten centimeter contours of modeled uplift are shown in black, and the peak appears to be offset ~4 km to the SW from the anticline but of similar along strike extent. Surface projections of outlines of the fault plane at depth at indicated by dashed black lines, and the updip surface project of the faults at depth to the surface are shown by solid black lines. (b) Comparison of modeled uplift (red) in the Khaki earthquake and contours of elevation (black, every 100 m), indicating the instantaneous earthquake-related uplift is not colocated with existing longer-term topographic high of the anticline.

mechanism is through fault-propagation fold growth driving the nonelastic deformation which must occur in the development of kilometer-scale folds (although at the regional scale the longer-wavelength folding is probably dominated by detachment folding over the weak Hormuz salt, Figure 3).

Alternatively, another possibility is that this anticline forms by fault bend folding, driven by slip on an underlying ramp and flat. Slip on the ramp produces uplift that is centered on one limb of the anticline, rather than
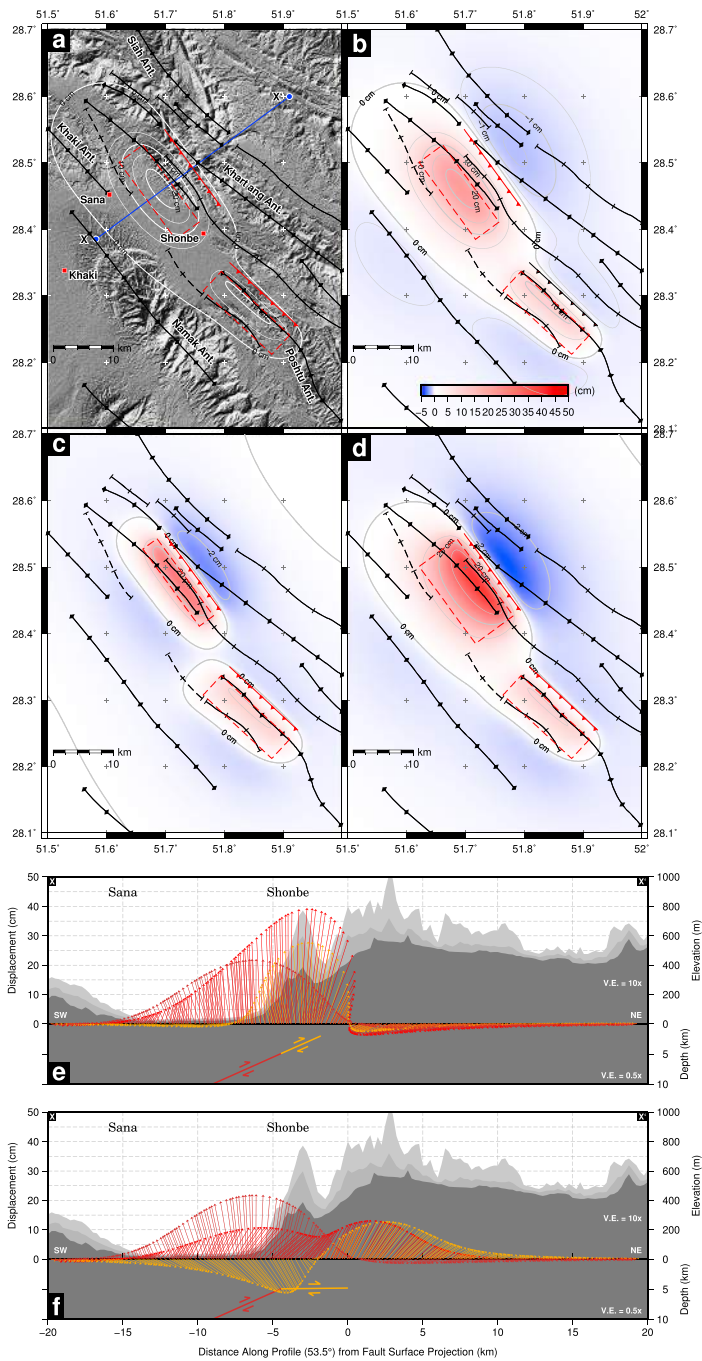
Figure 15. (a) SRTM 90 m hill-shaded relief (illumination from the SE). Surface projections of outlines of fault planes at depth are indicated by dashed red lines, and the updip surface projection of the faults at depth to the surface are shown by solid red lines. Surface traces of anticlines and synclines are marked by black lines with diamonds and ticks respectively. Cross section X–X′ shown in Figures 15e and 15f) is denoted by the blue line. (b) Regions of major uplift (red) and minor subsidence (blue) associated with the Khaki earthquake, based upon the uniform dislocation model determined here from the InSAR observations. Note the asymmetry in the color scale which is exaggerated by a factor of ten for the subsidence. (c) Synthetic uplift and subsidence patterns due to the same slip (0.8 m) on the updip portion of the NW segment over the depth range 5–2 km. (d) Combined uplift and subsidence patterns due to the same slip (0.8 m) on both the actual lower and hypothetical updip portion of the NW segment over the combined depth range 10–2 km. (e) Cross section perpendicular to the main segment showing profiles of topography. The ground motion from the slip on the deep fault surface from the Khaki earthquake is shown in brown. Ground motion for the shallow slip (orange vectors) and combined deep and shallow slip (red vectors) is overlaid. (f) Cross section perpendicular to the main segment showing ground motion from the slip on the deep fault (brown), on a subhorizontal section (orange) and the combined result (red), representing fault displacement along a fault-bend fold.
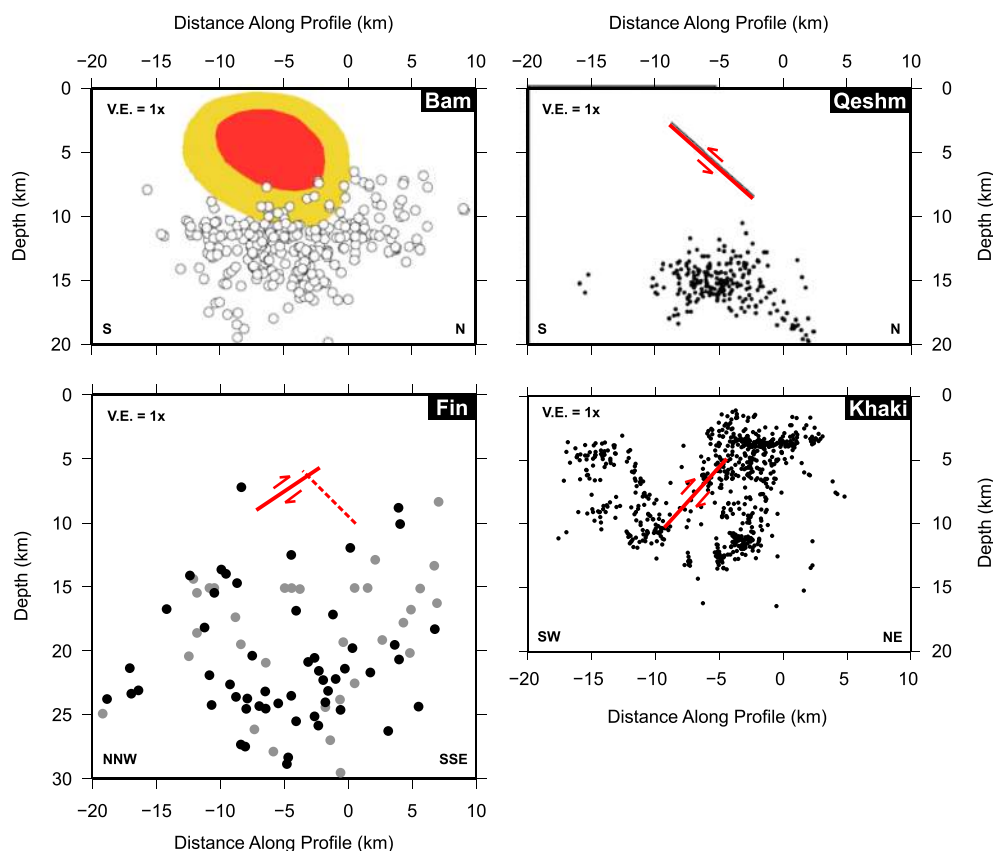
Figure 16. Comparison of the relative depth extents of InSAR determined fault slip and relocated aftershock depths in Khaki compared to that from the 2003 M_w 6.6 Bam earthquake [*Jackson et al.*, 2006], the Qeshm Island earthquake [*Nissen et al.*, 2010], and also the 2006 M_w 5.7 Fin (Iran) [*Roustaei et al.*, 2010] reverse faulting earthquake. Note also the near-horizontal 5–7 km long line of shallow seismicity to the NE of the upper portion of the Khaki fault plane at 4–5 km depth (bottom right).

on the anticline crest, and the anticline crest translates laterally (although the InSAR data are insensitive to this northeastward horizontal motion due to this being along-track). A similar mechanism was proposed for the 2006 M_w 5.7 Fin earthquake in the eastern Zagros [*Barnhart and Lohman*, 2013]. The subhorizontal line of seismicity which is distinguishable in the locally recorded aftershocks as emanating from the top of the main shock fault plane at 4–5 km depth (Figures 8 and 16) could be delineating such a structure. Figure 15f shows the displacement pattern if the slip continued along a subhorizontal plane at ∼5 km depth.

Observations of the postseismic deformation [*Copley and Reynolds*, 2014] following a set of three M_w 6 earthquakes in 1994 at Sefidebah, eastern Iran [*Parsons et al.*, 2006] showed long-lived afterslip motion contributing to the growth of topography. The aseismic slip in the case of Sefidebah was shallower than the buried coseismic slip and was still visible 16 years after the earthquake; the pattern of uplift following the long-term geomorphology. We suggest that shallower aseismic creep could also be one contributor to long-term topographic growth in the region of the Khaki earthquake.

The locations of the locally recorded aftershocks (Figure 8) delineate an overall NW-SE trend, parallel to folding, with a concentration of events in the northwest. We constructed two cross sections through the relocated data sets, perpendicular to the InSAR determined fault segments (Figure 8). For the northwestern segment, seismicity occurs over a depth range of 2–14 km but with relatively fewer events at 8–10 km indicating grouping at two independent depth intervals, with the bulk of the aftershocks in the competent sedimentary layer and a smaller concentration in the uppermost basement or lowermost cover (Figure 3). The aftershocks for the northwestern segment are clustered around the tips of the InSAR fault plane, and are fewer along the

rupture plane itself, as we would expect from the redistribution of stress, increasing failure at the ends of the fault.

By examining the relocated seismicity (Figure 6), we note that the main shock hypocenter and the M 3.9 foreshock 55 h earlier could be colocated within uncertainty, and are probably within a couple of kilometers of each other at most. This pair of events are also at the northern, lower end of the InSAR-determined fault segment, indicating updip and unilateral rupture to the SE. The largest aftershock (M_w 5.4, 14 h later) is located just over midway along the fault segment, 10 km southeast of the main shock hypocenter and initiating at a depth of about 8 km. Most of the recorded aftershocks are clustered around the northern segment and relative to the location of the InSAR imaged fault plane, cluster in the footwall rather than the hanging wall (Figure 6b). This is the same pattern as was found for the locally recorded 1 month aftershocks.

In addition to the longer-term postseismic motion following earthquakes, there is the potential for the stress changes following the main shock to also trigger large pulses of aseismic slip. However, the prevalence of these aseismic processes is debated [*Barnhart et al.*, 2013; *Nissen et al.*, 2014], in part because a limiting factor with the InSAR measurements are that they cover both the coseismic rupture and typically a few days to weeks following the earthquake, in which time further surface deformation can occur. In the case of the Khaki interferogram, a period of 2 weeks following the main shock is captured in the data, making it impossible to separate definitively the earthquake slip from postseismic motion with the InSAR alone. However, by combining the main shock epicenter relocation in the NW with the elongated InSAR deformation field and the short body waveform determined source time function, we can reason that the slip of the shallow southeastern segment was most likely triggered aseismically, although we cannot rule out that there was a large jump in the rupture between segments in an earthquake doublet as has been seen elsewhere (E. Nissen et al., Dynamic triggering of an earthquake doublet exposes limitations to rupture forecasting, in revision). The best fit source time function for the duration of rupture is 6 s (Figure 9). The epicentral relocation (section 3.1) places the hypocenter at the bottom NW corner of the fault plane (Figure 6) as imaged with InSAR (section 5). Taking a maximum rupture velocity of 3 km/s for this event in the sedimentary cover at 10 km depth to be at just below the shear-wave velocity (i.e., the Rayleigh wave speed = $0.92V_s$, Table 1), it would take 5.4 s to rupture the 16 km length of just the single NW segment (assuming no supershear rupture). It therefore seems likely that the second fault segment in the SE, constrained by the InSAR data to also be ~16 km in length, did not rupture in the main shock. Additionally, there are no large aftershocks relocated around the southern segment in the 2 weeks following the main shock that could result in seismic slip release consistent with the amount of deformation imaged.

We find in the slip models that the depth extent of rupture is tightly constrained, with narrow fault widths of 5–7 km compared to individual fault segment lengths of 16 km, giving a total rupture length of 32 km. Moreover, the depth extent of rupture for the individual two segments occurs over two mutually exclusive depth ranges (10–5 km and 4–2 km, Figure 13), which we can confidently resolve with the InSAR observations (Figures B5 and B6). These bottom depths of significant slip are at the shallower end of the distribution for a compilation of 13 M_w 6.0–7.2 earthquakes in Iran measured previously with InSAR [*Wright et al.*, 2013].

The thickness of the sedimentary cover, and therefore depth to basement, is less well constrained in the Khaki region of the Zagros than further east at Qeshm [*Nissen et al.*, 2010]. However, structural cross sections through the Khaki anticline (5 km to the NW of the Khaki epicenter, Figure 3 and marked in Figure 4) from *Oveisi et al.* [2009] (updated from *Sherkati et al.* [2006]) place the depth to basement at about 12 km. Additionally, a geological cross section from depth conversion of a seismic line running 30 km offshore from Khaki [*Perotti et al.*, 2011], places the basement at ~14 km.

This suggests a potential lithological control on the rupture extent, with the Hormuz Salt providing a bottom boundary to the limit of slip and the Cretaceous Kazhdumi mudstones providing a upper bound for the NW segment (Figure 3). The 5–7 km subhorizontal line of locally recorded aftershocks at 4–5 km depth connects with the updip end of the coseismic rupture and may be picking out a particular weak lithological horizon (Figures 8 and 16). The controls on the distribution of slip for the southeastern segment are less clear but could be related to the distribution of the marls of the Gurpi-Pabdeh Formations (Figure 17) over the depth range of 2–4 km. The depth range and likely rheology of these formations could explain the southeastern segment's narrow 2 km width of 20–40 cm slip running for 16 km and its potential aseismic behavior.
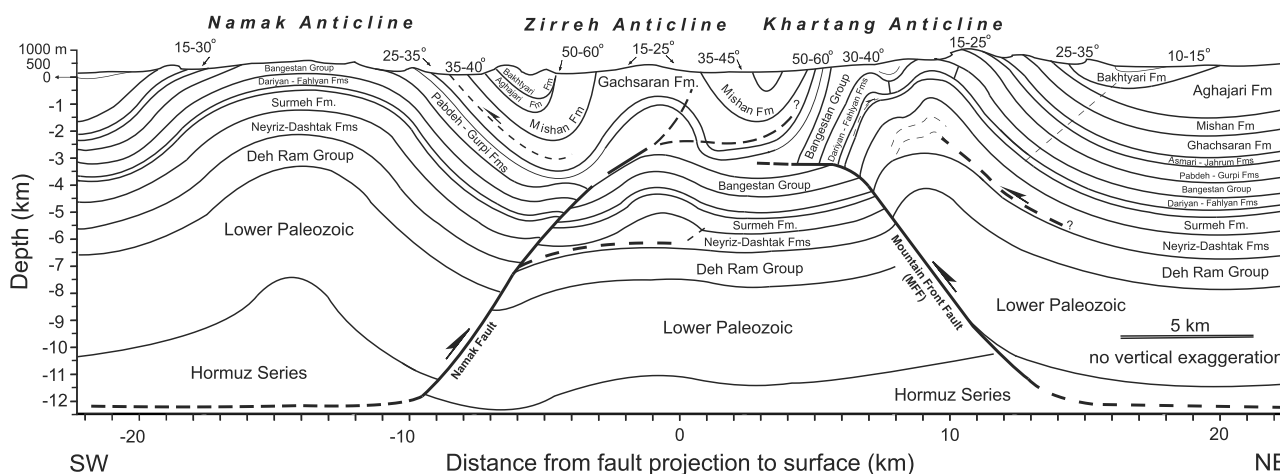
Figure 17. Structural cross section showing the faulting and anticlines along a section through the center of the southeastern fault segment (section Y–Y' in Figure 11) based upon surface geology constructed using constant thickness of lithologies (except for more deformable layers) and other structural sections in the area [*Oveisi et al.*, 2009]. See Figure 2 for lithologies and ages.

Similar patterns of vertical slip segmentation were observed in recent reverse faulting earthquakes in China, Turkey, and Nepal [*Elliott et al.*, 2011, 2013, J. R. Elliott, et al., Himalayan megathrust geometry and relation to topography revealed by the Gorkha Earthquake, in revision] implying that large (M_w 6.2–7.8) continental earthquakes do not necessarily rupture the entire seismogenic crust if there are structural or lithological barriers to coseismic slip. Similarly, slip over different depth intervals was observed on the Gowk fault in southeast Iran: the 1981 M_w 7.1 Sirch earthquake was relatively deep (centroid depth ~18 km) with little measurable fault surface offset [*Berberian et al.*, 1984], while the shallower (~5 km) 1998 M_w 6.6 Fandoqa earthquake reruptured the southern portion of this fault 17 years later [*Berberian et al.*, 2001]. In the Zagros, the presence of several weak units within and at the base of the sedimentary cover may help explain why earthquakes here are mostly limited to moderate magnitudes of M_w ~6 or less [*Nissen et al.*, 2011].

Taken together with the aftershock locations showing earthquakes occurring over a larger depth range than the InSAR slip, these observations reinforce recent assertions for other earthquakes in the Zagros [*Nissen et al.*, 2010; *Roustaei et al.*, 2010] that the main shock rupture occurs in the sedimentary cover (potentially nucleating toward the bottom of the cover as appears to be the case here) and causes aftershocks in rocks adjacent to and interbedded with the Hormuz salt and other layers below [*Nissen et al.*, 2014], leaving the shortening in the basement to occur largely aseismically (though a few resolvable basement earthquakes have been measured in the Simply Folded Belt) [*Nissen et al.*, 2011; *Allen et al.*, 2013].

The aftershocks observed in the first (2005 M_w 5.8) of the Qeshm Island earthquake sequence [*Nissen et al.*, 2010], in the 2006 M_w 5.7 Fin earthquake [*Roustaei et al.*, 2010], and in the 2003 M_w 6.6 Bam earthquake [*Jackson et al.*, 2006] were constrained to lie almost entirely below the InSAR determined fault plane (Figure 16). However, in contrast, the Khaki aftershocks occurred over a wider range than the depth interval of the coseismic slip (although centered at the same depth). Further examples of deeper aftershocks beneath the imaged shallow slip region are seen for the 2008 M_w 7.2 Iwata-Miyagi reverse faulting earthquake in Japan [*Takada et al.*, 2009], the 2000 M_w 6.8 Tottori (Japan) [*Semmane et al.*, 2005], and the 2008 M_w 7.9 Wenchuan (China) [*Tong et al.*, 2010] earthquakes. Therefore, the use of aftershock locations to delimit the main shock rupture extent can lead to the incorrect assignment in depth (and potentially length) of the zone of significant slip, in some cases apportioning the slip too deep [*Nissen et al.*, 2014], or as in this Khaki case, over a much wider depth interval than the significant coseismic slip has been imaged geodetically.

7. Conclusions

We produce a two-segment reverse fault model that closely matches InSAR observations of ground deformation in the 2013 Khaki earthquake. The two segments ruptured different depth intervals, but in each case slip was restricted to narrow (<5 km) vertical limits considering the ~16 km segment lengths. Significant reverse
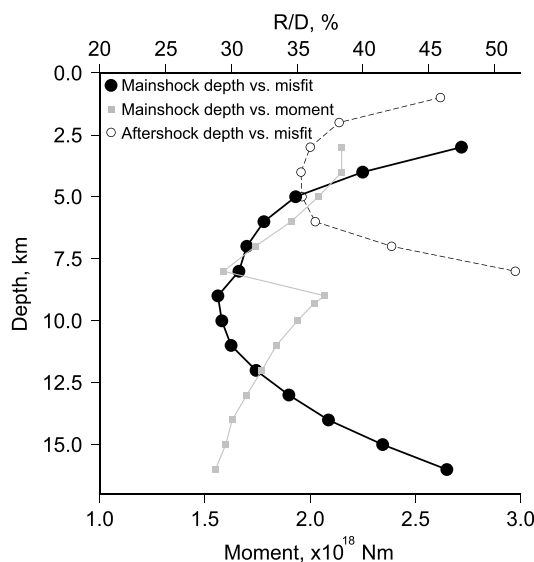
Figure A1. Body-waveform misfit versus centroid depth (black line). The minimum misfit is at 9 km but the increase in misfit to the seismograms is less than 15% over the depth interval 6–12 km. The trade-off curve for the M_W 5.4 aftershock is shown be the dashed line with a minimum at a centroid depth of 5 km. The trade-off in moment with depth is shown by the grey line for the main shock. The discontinuity in moment and misfit at 8 km are the result of the boundary in the velocity model at this depth.

slip occurred perhaps exclusively, or at least predominantly, in the sedimentary cover (<11 km). The bottom extent of slip is most likely controlled by the Hormuz salt and the upper extent of slip on the main NW segment is likely controlled by the Kazhdumi Formation at about 5 km. There is a lack of clear surface rupture associated with the main fault segments of the M_w 6.2 earthquake, confirming a buried source. Earthquake relocations are clustered mainly around the NW segment, over a depth range wider than the coseismic fault plane. The relocated hypocenter is at the northern end of this NW segment at a depth equivalent to the bottom of a SW dipping plane constrained with InSAR. The positioning of the hypocenter at the northwest end of the faulting indicates rupture propagation from NW to SE, updip through the sedimentary cover. Given the combined length of the two fault segments and short source time function, we reason that both segments could not have ruptured in the main shock. With no sufficiently large aftershocks located around the southeastern segment to explain the displacements in this area, it is likely that this segment slipped

mostly aseismically sometime in the 2 week period after the main shock that the InSAR data cover. The main uplift pattern from this event is parallel to, but centered, 3 km SW of the nearest anticline axis, indicating either that shallower slip drives the location and growth of this anticline in the longer term or, alternatively, that this anticline is controlled by slip on an underlying ramp and flat structure.

Appendix A: Body Waveform Analysis

The body waveform analysis of the Khaki earthquake and largest aftershock is discussed in section 3.3. The body waveform misfit versus centroid depth is shown in Figure A1, and the aftershock focal mechanism is shown in Figure A2.

Appendix B: InSAR Methods

We used SAR measurements from a descending track of the Canadian Space Agency (CSA) RADARSAT-2 C band ($\lambda = 5.65$ cm) instrument (with a center scene angle of incidence of 23°). The interferogram covers the 9 April 2013 main shock and largest aftershock and was created from SAR acquisitions from 12 October 2012 and 24 April 2013. The data were processed using the GAMMA software using updated orbits from CSA and multilooked to five looks in azimuth. The topographic phase contribution was removed using the 3-arcsec SRTM DEM. The interferograms were then filtered using a power spectrum filter [*Goldstein and Werner*, 1998] and unwrapped using a minimum cost flow (MCF) algorithm. Finally, the interferogram was geocoded and reprojected to the local UTM coordinate system (39 N) with an 80 m resolution.

The analysis performed on the InSAR data to determine the fault geometry and distribution of slip follows similar approaches taken in *Elliott et al.* [2011], using the algorithms developed by *Wright et al.* [1999]; *Funning et al.* [2005]. We briefly summarize the methodology here before moving onto the uncertainty and resolution analysis.

We make use of the high degree of spatial correlation within an interferogram [*Hanssen*, 2001] to downsample the interferogram that originally consisted of several million measurements of ground displacement in the line of sight from the satellite using a quadtree approach [e.g., *Jonsson et al.*, 2002], which samples the data more heavily in regions of high-phase gradient near the fault (Figure B4). The geodetic measurements in the

Aftershock (10 April)
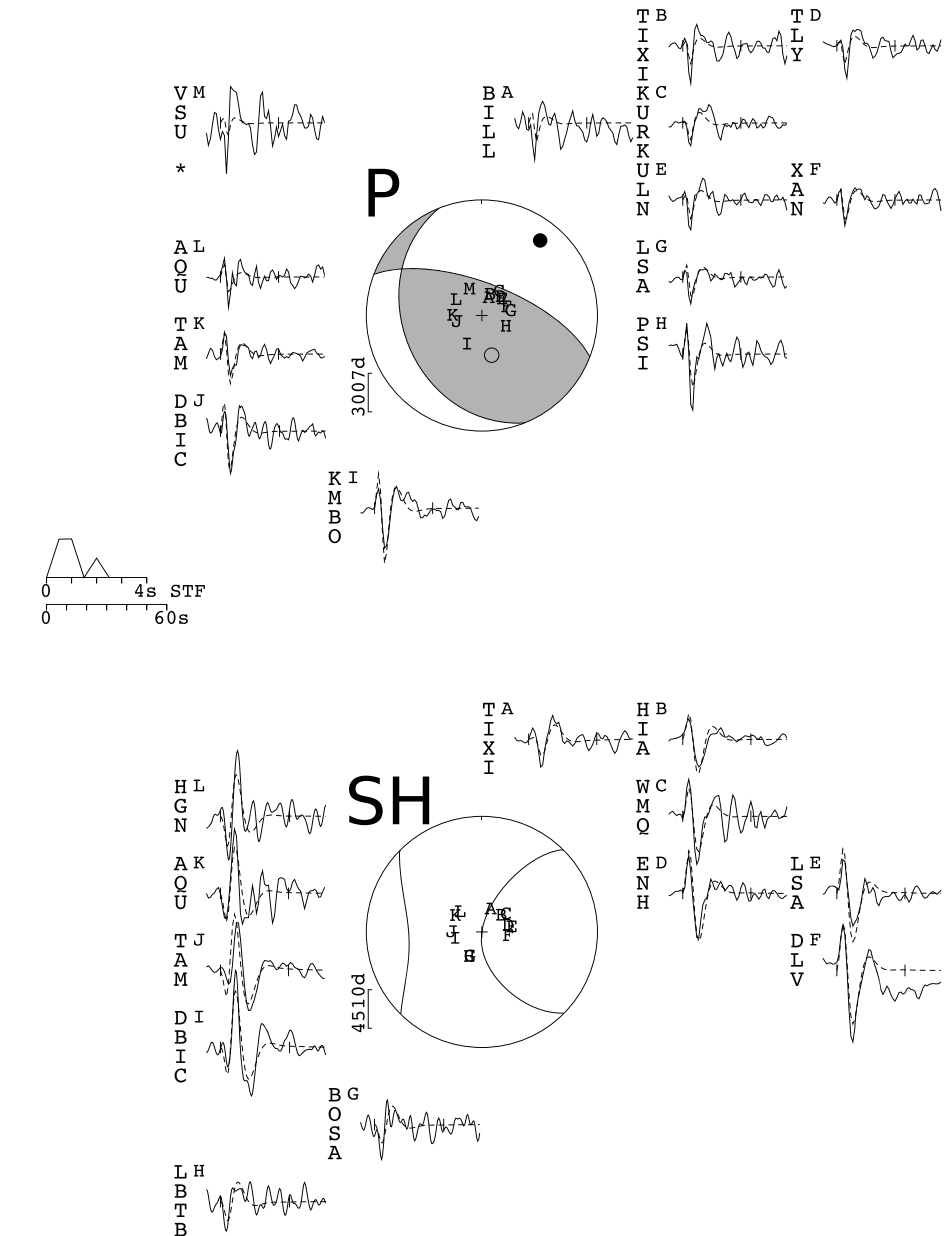### 158/32/133/4/1.4E17

Figure A2. Khaki aftershock body-waveform minimum misfit solutions from the inversion of *P* and SH body waves for a point source in a half-space. Rest of caption as for Figure 9.

near-field will have a greater sensitivity to the earthquake mechanism and slip than those in the far-field, so we sample a higher density of displacements above the fault rupture area. This procedure resulted in almost ~2500 line-of-sight displacements as input into our inversion procedure and which are equally weighted.

We use the expressions given in *Okada* [1985] to model the downsampled InSAR ground displacements as resulting from slip on rectangular fault planes behaving as dislocations in an assumed uniform elastic half-space. The values for the Lamé elastic parameters of this half-space are taken to be $\lambda = \mu = 2.2 \times 10^{10}$ Pa. These values are consistent with the best estimates of average seismic velocities used in the body waveform inversion for consistency and to allow comparisons between estimates of moment release.
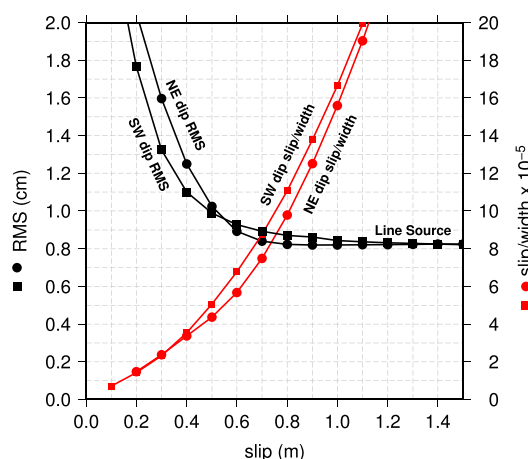
Figure B1. RMS misfit curve (black) to the downsampled InSAR data for varying choices of slip on the NW fault segment while other fault parameters (apart from location) are free, for an assumed SW dipping (circles) and NE dipping (squares) segment. The slip-to-width ratios for each choice of dip orientation are shown in red (right-hand axis).

We using a nonlinear downhill Powell's algorithm with multiple Monte Carlo restarts to avoid local minima [*Press et al.*, 1992; *Wright et al.*, 1999] to invert the downsampled interferometric data set for uniform slip on the two fault segments. For each of the fault segments, the source parameters are strike, dip, rake, slip, surface center location, length, and top and bottom depth (Table 3). However, it was necessary to fix the position of the fault segments in the two-segment model using the distribution of fringes and to also set the slip on the northwest segment as explained in the main text as the geometry collapses to a line source and the slip becomes unreasonably large (Figure B1). In order to account for the choice of unwrapping point and orbital errors, we also solve for the nuisance parameters of a static line-of-sight shift and linear gradients in phase of the interferogram. As discussed in section 5, the difference in misfit to the InSAR data is almost indistinguishable between solving for the geometry with the NE and SW dipping fault plane solutions (compare Figure 11 with Figure B2), so we are unable to determine the focal plane ambiguity with InSAR alone and instead rely on noting that only the SW dipping fault plane is consistent with the hypocentral relocation analysis for the main shock.

Using the geometry constrained to that found in the uniform slip modeling, we also carried out linear inversions in which the slip was allowed to vary with position on the two fault segments. Each segment was subdivided into an array of rectangular 1 km length by 1 km depth slip patches. We solved for slip on each segment (Figure 12a), as well as the nuisance parameters, following the method of *Du et al.* [1992]; *Jonsson et al.* [2002]; *Wright et al.* [2003]; *Funning et al.* [2005]. In order to regularize the inverse problem, a finite-difference Laplacian smoothing constraint was applied to the slip solution in addition to a positivity constraint. The choice of smoothing factor depends on a trade-off between decreasing the fault slip roughness and minimizing the increase in RMS misfit as a result of the increased smoothing [*Wright et al.*, 2004]. We have aimed to minimize the level of smoothing to increase the resolution of the slip gradients at depth without introducing spurious slip patches of large magnitude.

We perturb the downsampled interferogram data set with random synthetic correlated noise in order to perform a Monte Carlo analysis, to estimate the uncertainties in slip magnitude in the distributed slip models [*Wright et al.*, 2003; *Funning et al.*, 2005]. We generate 100 data sets perturbed with noise of the correct statistical properties and carry out the inversion on each of the 100 perturbed data sets to estimate the standard deviation in slip (Figure 12e). In order to simulate the noise we sample a far-field portion of the full-resolution interferogram and calculate its autocovariance function [*Hanssen*, 2001; *Lohman and Simons*, 2005b; *Wright et al.*, 2004], to which a 1-D covariance model is fitted to estimate the variance and decay distance of the noise. The uncertainties derived from Monte Carlo modeling do not account for errors in our assumptions about choice of fault location, segmentation, or data sampling. It is also possible to examine the uncertainties (Table 3) and trade-offs between the parameters left free in the uniform slip inversion (Figure B3), using the same set of perturbed input data.
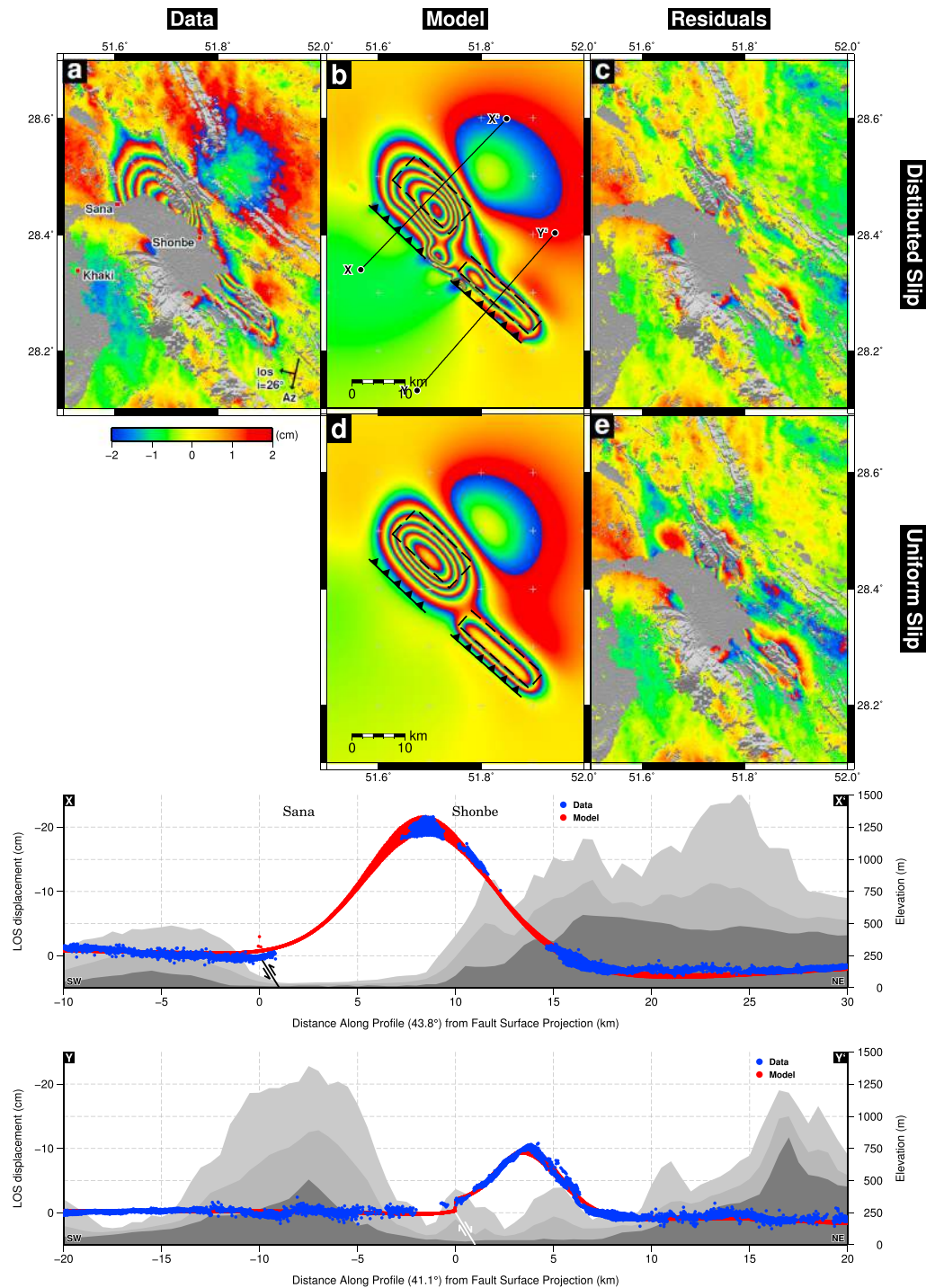
Figure B2. Interferogram, models and residuals based upon distributed and uniform slip modeling for the Khaki earthquake, assuming NE dipping fault planes. Colors show range changes as fringes rewrapped to 4 cm, with color cycles blue through yellow to red indicating motion away from the satellite. The updip projection of the fault segments are marked by the pair of barbed solid lines (triangles on the hanging wall) and the surface outline of the uniform slip regions by dashed rectangles. The satellite track azimuths (Az) and line-of-sight directions (LOS) with angle of incidence (i) are indicated by black arrows. Profile X–X' through the RADARSAT-2 data, model, and topography is shown at the bottom. The profile is taken perpendicular to the strike of the fault segments. InSAR displacements are represented by blue dots, the modeled data projected into the same line-of-sight by red dots. Profiles of topography are taken from the SRTM 3 second data along the same sections, sampling 10 km wide swaths and showing minimum (dark grey), mean (grey), and maximum (light grey) elevations. The line-of-sight displacement axis has been inverted, so negative motion (which is toward the satellite and mainly uplift in this case) is to the top of the figure.
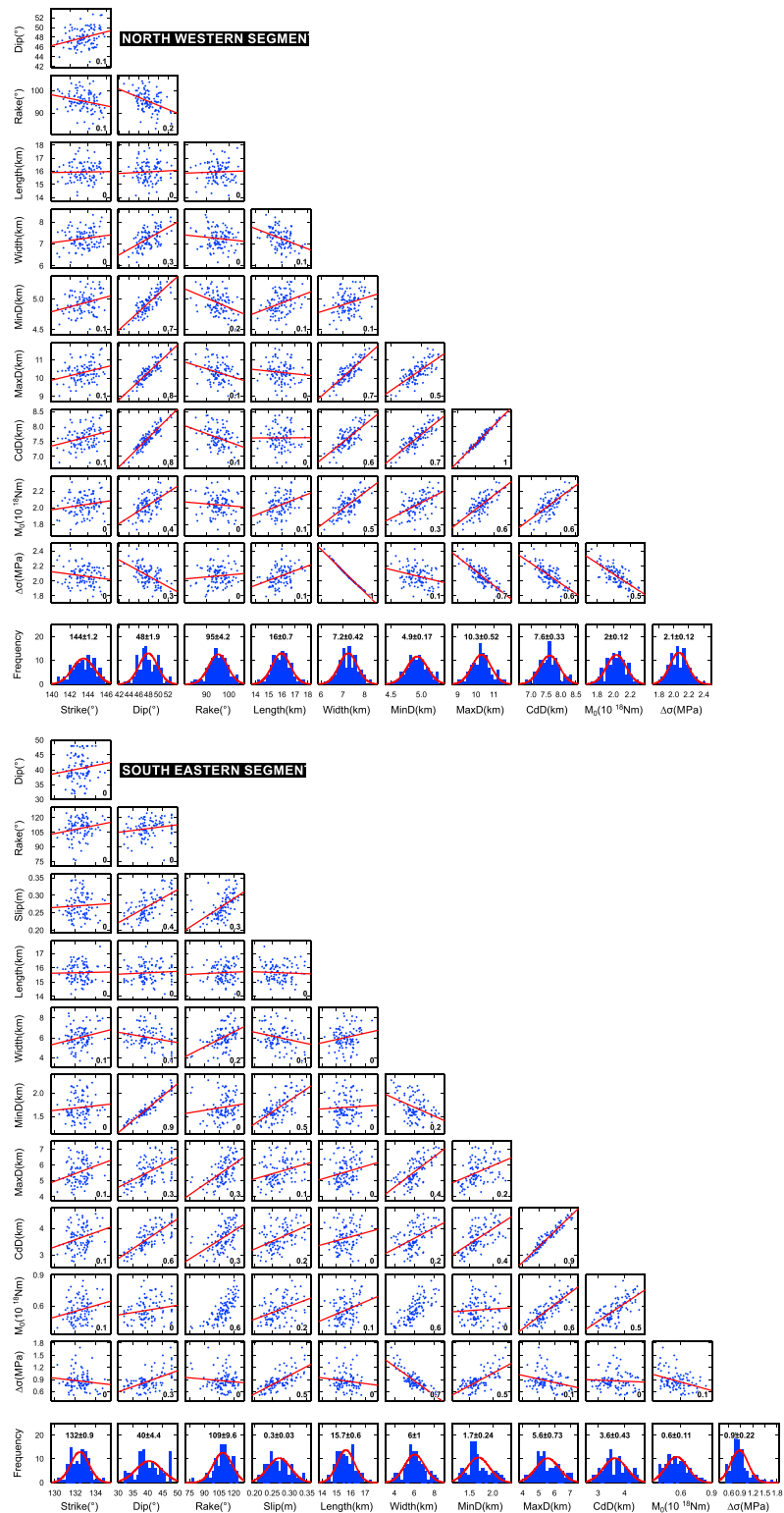
Figure B3. Fault parameter trade-offs for the uniform-slip two-segment model of the Khaki earthquake. Each of the 100 dots in the upper plots is the best fit solution for one data set to which Monte Carlo; spatially correlated noise has been added to each interferogram based upon the far-field noise. The line indicates the linear regression, with the number in the lower right corner indicating the correlation coefficient. Histograms summarize the distribution for each parameter, with the mean and standard deviation value given above and the normal distribution fit shown by the red curve. The minimum (MinD), maximum (MaxD), and Centroid (CdD) depths are given as well as the moment (Mo) and Stress Drop ($\Delta\sigma$).
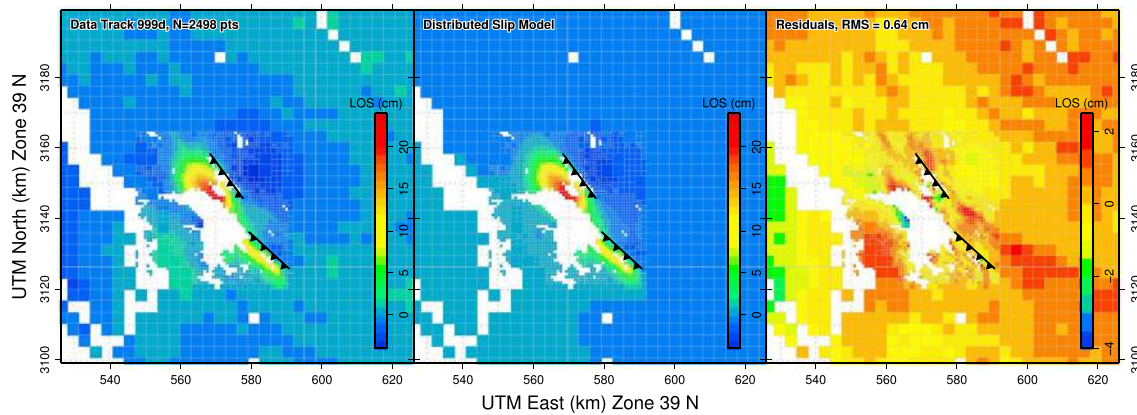
Figure B4. Downsampled interferogram data, model, and residuals for the RADARSAT-2 track for (top) uniform and (bottom) distributed slip in UTM coordinates Zone 39 North. Values are unwrapped line-of-sight displacements with positive (red) indicating motion toward the satellite. Cell sizes varying from 0.8 km in the near-field to 3.2 km in the far-field.

Using the fault geometry of the two segments determined from uniform slip modeling (Table 3), we forward model known checker-board slip distributions with a range of subfault patch sizes from ~2–5 km, with alternating slip values of 0 m and 0.5 m (Figure B5). These forward models are then masked so as to exclude displacements from regions that are incoherent in the real interferograms, downsampled to the same number and location of points as for the real data (Figure B4), and used to invert for the known checker-board slip distribution. This procedure helps illustrate how well differing regions of slip are resolved over the various depth ranges. The results (Figure B5) indicate 2–3 km patches can only be resolved at best in the upper 4 km, while 4–5 km patches are resolvable at 10 km. Therefore, given the slip extent of the main slip patch on the
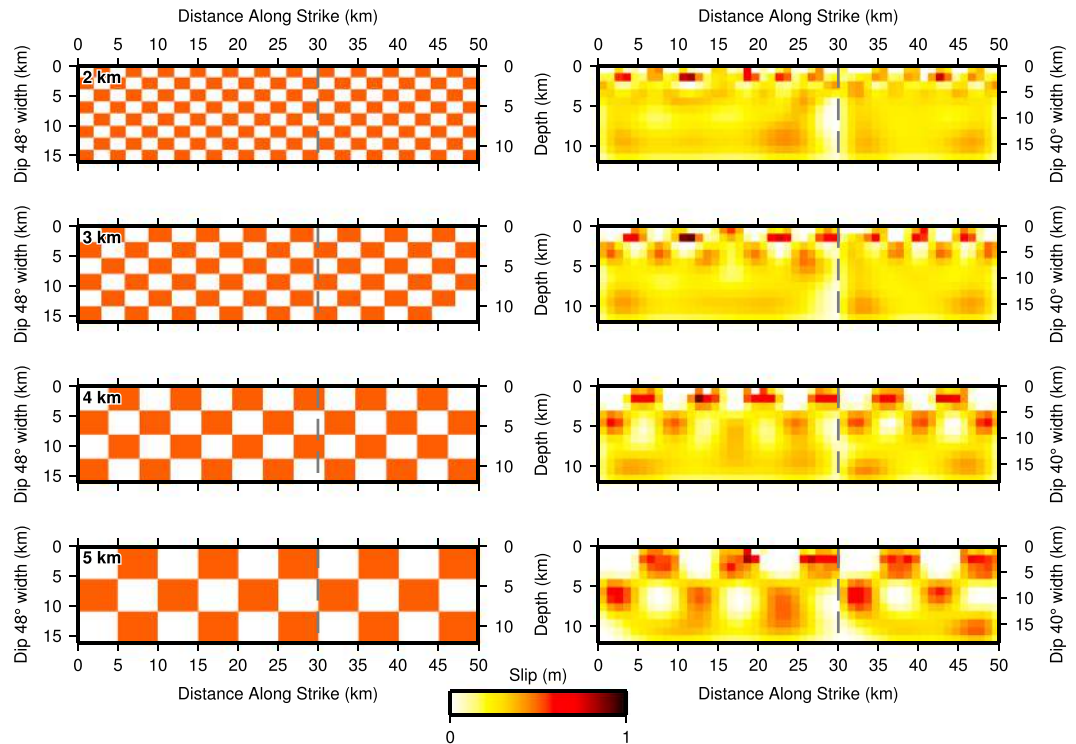

Figure B5. Checker-board tests for a range of sub-fault sizes from ~2–5 km with (left column) fixed 0.5 m slip patches, generated on the same two-fault segment geometry as that in the earthquake model. The (right column) resulting slip distributions are from inverting the forward-generated models of surface deformation masked to the same coverage of SAR data and downsampled with same spatial distribution of points as that used for the real deformation data set (Figure B4). Note the outer *y* axis distance scale is downdip width which varies for the two differently dipping segments, while the inner scale is depth down to 12 km.
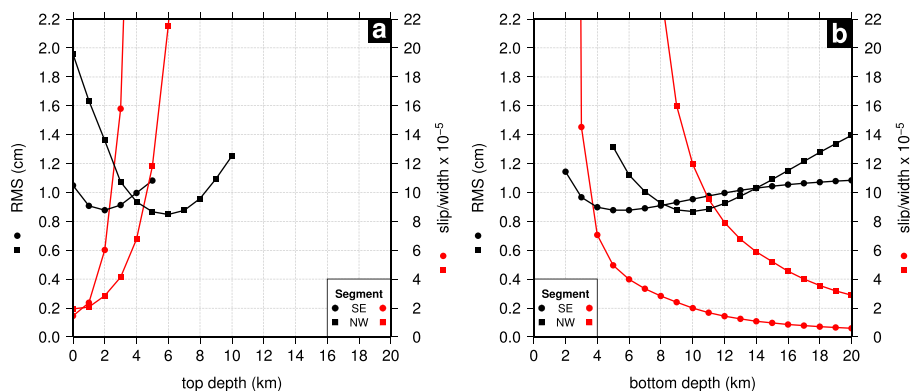
Figure B6. (a) RMS well for the InSAR data with varying the top depth of each segment used in the uniform slip inversions with the slip, moment, strike, dip, and rake permitted to vary (black line and dots/squares). The RMS minimum is at a top depth of 2 and 6 km for the southeast and northwest segment, respectively. Increasing or decreasing the depth of the top extent of faulting by more than 1 km increases the RMS significantly. The red line and circles show the slip-to-fault width ratio for each solution. Top depths deeper than the best fit solutions also start to have increasingly unrealistic large slip-to-width ratios as the solution approaches a line source. (b) As for Figure B6a, except that the bottom depth for each segment in turn is now varied in 1 km intervals.

northwest segment is 5 km in depth and 16 km in length, we are able to resolve gradients at the top (5 km) and bottom (10 km) of this segment. We are therefore confident of the narrow depth intervals over which significant fault slip has occurred on these two segments.

We also explore the change in the misfit to the InSAR data resulting from fixing in turn the top and bottom fault depth at 1 km intervals for each segment separately in the uniform slip modeling (allowing slip, moment, strike, dip, and rake to vary and keeping the fault location fixed to that used for the slip models given in Table 3). The well-defined minimum misfit for the bottom depth of the main northwest segment is at 8–12 km (Figure B6), with a significant increase in RMS seen as we attempt to force the slip either shallower by more than a couple of kilometers and deeper by more than a few. The top depths for both segments are even more tightly bound in narrow rms wells at 2 and 6 km.

References

Adams, A., R. Brazier, A. Nyblade, A. Rodgers, and A. Al-Amri (2009), Source parameters for moderate earthquakes in the Zagros mountains with implications for the depth extent of seismicity, *Bull. Seismol. Soc. Am.*, 99, 2044–2049, doi:10.1785/0120080314.

Allen, M. B., and H. A. Armstrong (2008), Arabia Eurasia collision and the forcing of mid-Cenozoic global cooling, *Palaeogeogr. Palaeoclimatol. Palaeoecol.*, 265, 52–58.

Allen, M. B., C. Saville, E. J.-P. Blanc, M. Talebian, and E. Nissen (2013), Orogenic plateau growth: Expansion of the Turkish-Iranian Plateau across the Zagros fold-and-thrust belt, *Tectonics*, 32, 171–190, doi:10.1002/tect.20025.

Ambraseys, N. N., and C. P. Melville (1982), *A History of Persian Earthquakes*, Cambridge Univ. Press, Cambridge, U. K.

Authemayou, C., D. Chardon, O. Bellier, Z. Malekzadeh, E. Shabanian, and M. R. Abbassi (2006), Late Cenozoic partitioning of oblique plate convergence in the Zagros fold-and-thrust belt (Iran), *Tectonics*, 25, C3002, doi:10.1029/2005TC001860.

Authemayou, C., O. Bellier, D. Chardon, L. Benedetti, Z. Malekzade, C. Claude, B. Angeletti, E. Shabanian, and M. R. Abbassi (2009), Quaternary slip-rates of the Kazerun and the Main Recent Faults: Active strike-slip partitioning in the Zagros fold-and-thrust belt, *Geophys. J. Int.*, 178, 524–540, doi:10.1111/j.1365-246X.2009.04191.x.

Baker, C., J. Jackson, and K. Priestley (1993), Earthquakes on the Kazerun Line in the Zagros Mountains of Iran: Strike-slip faulting within a fold-and-thrust belt, *Geophys. J. Int.*, 115, 41–61, doi:10.1111/j.1365-246X.1993.tb05587.x.

Barnhart, W. D., and R. B. Lohman (2013), Phantom earthquakes and triggered aseismic creep: Vertical partitioning of strain during earthquake sequences in Iran, *Geophys. Res. Lett.*, 40, 819–823, doi:10.1002/grl.50201.

Barnhart, W. D., R. B. Lohman, and R. J. Mellors (2013), Active accommodation of plate convergence in Southern Iran: Earthquake locations, triggered aseismic slip, and regional strain rates, *J. Geophys. Res. Solid Earth*, 118(10), 5699–5711, doi:10.1002/jgrb.50380.

Berberian, M. (1995), Master blind thrust faults hidden under the Zagros folds: Active basement tectonics and surface morphotectonics, *Tectonophysics*, 241, 193–224.

Berberian, M., and D. Papastamatiou (1978), Khurgu (north Bandar Abbas, Iran) earthquake of March 21, 1977: A preliminary field report and a seismotectonic discussion, *Bull. Seismol. Soc. Am.*, 68(2), 411–428.

Berberian, M., J. A. Jackson, M. Ghorashi, and M. H. Kadjar (1984), Field and teleseismic observations of the 1981 Golbaf-Sirch earthquakes in SE Iran, *Geophys. J. Int.*, 77, 809–838, doi:10.1111/j.1365-246X.1984.tb02223.x.

Berberian, M., J. A. Jackson, E. Fielding, B. E. Parsons, K. Priestley, M. Qorashi, M. Talebian, R. Walker, T. J. Wright, and C. Baker (2001), The 1998 March 14 Fandoqa earthquake (M_w 6.6) in Kerman province, southeast Iran: Re-rupture of the 1981 Sirch earthquake fault, triggering of slip on adjacent thrusts and the active tectonics of the Gowk fault zone, *Geophys. J. Int.*, 146, 371–398, doi:10.1046/j.1365-246X.2001.01459.x.

Burberry, C. M., J. W. Cosgrove, and J. G. Liu (2008), Spatial arrangement of fold types in the Zagros Simply Folded Belt, Iran, indicated by landform morphology and drainage pattern characteristics, *J. Maps*, 4(1), 417–430.

Carruba, S., C. R. Perotti, R. Buonaguro, R. Calabrò, R. Carpi, and M. Naini (2006), Structural pattern of the Zagros fold-and-thrust belt in the Dezful Embayment (SW Iran), *Geol. Soc. Am. Spec. Pap.*, *414*, 11–32.

Casciello, E., J. Vergés, E. Saura, G. Casini, N. Fernández, E. Blanc, S. Homke, and D. W. Hunt (2009), Fold patterns and multilayer rheology of the Lurestan Province, Zagros Simply Folded Belt (Iran), *J. Geol. Soc. London*, *166*, 947–959.

Colman-Sadd, S. P. (1978), Fold development in Zagros simply folded belt, Southwest Iran, *Am. Assoc. Petrol. Geol. Bull.*, *62*, 984–1003.

Copley, A., and K. Reynolds (2014), Imaging topographic growth by long-lived postseismic afterslip at Sefidabeh, east Iran, *Tectonics*, *33*, 330–345, doi:10.1002/2013TC003462.

Copley, A., E. Karasozen, B. Oveisi, J. R. Elliott, S. Samsonov, and E. K. Nissen (2015), Seismogenic faulting of the sedimentary sequence and laterally-variable material properties in the Zagros Mountains (Iran) revealed by the August 2014 Murmuri (Dehloran) earthquake sequence, *Geophys. J. Int.*, *203*, 1436–1459, doi:10.1093/gji/ggv365.

Daniell, J. E., B. Khazai, F. Wenzel, and A. Vervaeck (2011), The CATDAT damaging earthquakes database, *Nat. Hazards Earth Syst. Sci.*, *11*, 2235–2251, doi:10.5194/nhess-11-2235-2011.

Du, Y., A. Aydin, and P. Segall (1992), Comparison of various inversion techniques as applied to the determination of a geophysical deformation model for the 1983 Borah Peak earthquake., *Bull. Seismol. Soc. Am.*, *82*, 1840–1866.

Dziewonski, A. M., and J. H. Woodhouse (1983), An experiment in systematic study of global seismicity Centroid-moment tensor solutions for 201 moderate and large earthquakes of 1981, *J. Geophys. Res.*, *88*, 3247–3271, doi:10.1029/JB088iB04p03247.

Ekström, G., A. M. Dziewoński, N. N. Maternovskaya, and M. Nettles (2005), Global seismicity of 2003: Centroid moment-tensor solutions for 1087 earthquakes, *Phys. Earth Planet. Inter.*, *148*, 327–351, doi:10.1016/j.pepi.2004.09.006.

Elliott, J. R., B. Parsons, J. A. Jackson, X. Shan, R. A. Sloan, and R. T. Walker (2011), Depth segmentation of the seismogenic continental crust: The 2008 and 2009 Qaidam earthquakes, *Geophys. Res. Lett.*, *38*, L06305, doi:10.1029/2011GL046897.

Elliott, J. R., E. K. Nissen, P. C. England, J. A. Jackson, S. Lamb, Z. Li, M. Oehlers, and B. Parsons (2012), Slip in the 2010–2011 Canterbury earthquakes, New Zealand, *J. Geophys. Res.*, *117*, B03401, doi:10.1029/2011JB008868.

Elliott, J. R., A. C. Copley, R. Holley, K. Scharer, and B. Parsons (2013), The 2011 Mw 7.1 Van (Eastern Turkey) earthquake, *J. Geophys. Res. Solid Earth*, *118*, 1619–1637, doi:10.1002/jgrb.50117.

Fakhari, M. D., G. J. Axen, B. K. Horton, J. Hassanzadeh, and A. Amini (2008), Revised age of proximal deposits in the Zagros foreland basin and implications for Cenozoic evolution of the High Zagros, *Tectonophysics*, *451*, 170–185.

Funning, G. J., B. Parsons, T. J. Wright, J. A. Jackson, and E. J. Fielding (2005), Surface displacements and source parameters of the 2003 Bam (Iran) earthquake from Envisat advanced synthetic aperture radar imagery, *J. Geophys. Res.*, *110*, B09406, doi:10.1029/2004JB003338.

Ghods, A., M. Rezapour, E. Bergman, G. Mortezanejad, and M. Talebian (2012), Relocation of the 2006 Mw 6.1 Silakhour, Iran, Earthquake Sequence: Details of Fault Segmentation on the Main Recent Fault, *Bull. Seismol. Soc. Am.*, *102*, 398–416, doi:10.1785/0120110009.

Goldstein, R. M., and C. L. Werner (1998), Radar interferogram filtering for geophysical applications, *Geophys. Res. Lett.*, *25*, 4035–4038, doi:10.1029/1998GL900033.

Hanssen, R. F. (2001), *Radar Interferometry: Data Interpretation and Analysis*, Kluwer Acad., Norwell, Mass.

Hatzfeld, D., M. Tatar, K. Priestley, and M. Ghafory-Ashtiany (2003), Seismological constraints on the crustal structure beneath the Zagros Mountain belt (Iran), *Geophys. J. Int.*, *155*, 403–410, doi:10.1046/j.1365-246X.2003.02045.x.

Hayes, G. P., L. Rivera, and H. Kanamori (2009), Source inversion of the W-phase: Real-time implementation and extension to low magnitudes, *Seismol. Res. Lett.*, *80*(5), 817–822.

Hessami, K., H. A. Koyi, and C. J. Talbot (2001a), The significance of strike-slip faulting in the basement of the Zagros fold and thrust belt, *J. Petr. Geol.*, *24*, 5–28.

Hessami, K., H. A. Koyi, C. J. Talbot, H. Tabasi, and E. Shabanian (2001b), Progressive unconformities within an evolving foreland fold thrust belt, Zagros Mountains, *J. Geol. Soc. London*, *158*, 969–981.

Jackson, J., and T. Fitch (1981), Basement faulting and the focal depths of the larger earthquakes in the Zagros mountains (Iran), *Geophys. J. Int.*, *64*, 561–586, doi:10.1111/j.1365-246X.1981.tb02685.x.

Jackson, J., and D. McKenzie (1988), The relationship between plate motions and seismic moment tensors, and the rates of active deformation in the Mediterranean and Middle East, *Geophys. J. Int.*, *93*, 45–73, doi:10.1111/j.1365-246X.1988.tb01387.x.

Jackson, J., et al. (2006), Seismotectonic, rupture process, and earthquake-hazard aspects of the 2003 December 26 Bam, Iran, earthquake, *Geophys. J. Int.*, *166*, 1270–1292, doi:10.1111/j.1365-246X.2006.03056.x.

Jackson, J. A. (1980), Reactivation of basement faults and crustal shortening in orogenic belts, *Nature*, *283*, 343–346, doi:10.1038/283343a0.

Jahani, S. (2008), Tectonique salifère, plissement et fracturation dans les provinces du Fars Oriental et le domaine marin adjacent du Golfe Persique (Iran), PhD thesis, Université de Cergy-Pontoise, Cergy, France.

Jahani, S., J.-P. Callot, D. Frizon de Lamotte, J. Letouzey, and P. Leturmy (2007), The salt diapirs of the Eastern Fars Province (Zagros, Iran): A brief outline of their past and present, in *Thrust Belts and Foreland Basins*, pp. 289–308, Springer, Berlin Heidelberg., doi:10.1007/978-3-540-69426-7.

Jahani, S., J.-P. Callot, J. Letouzey, and D. Frizon de Lamotte (2009), The eastern termination of the Zagros Fold-and-Thrust Belt, Iran: Structures, evolution, and relationships between salt plugs, folding, and faulting, *Tectonics*, *28*, TC6004, doi:10.1029/2008TC002418.

Jonsson, S., H. Zebker, P. Segall, and F. Amelung (2002), Fault slip distribution of the M_w 7.2 Hector Mine earthquake estimated from satellite radar and GPS measurements, *Bull. Seismol. Soc. Am.*, *92*, 1377–1389, doi:10.1785/0120000922.

Jordan, T. H., and K. A. Sverdrup (1981), Teleseismic location techniques and their application to earthquake clusters in the south-central Pacific, *Bull. Seismol. Soc. Am.*, *71*(4), 1105–1130.

Kanamori, H., and L. Rivera (2008), Source inversion of W phase: Speeding up seismic tsunami warning, *Geophys. J. Int.*, *175*, 222–238, doi:10.1111/j.1365-246X.2008.03887.x.

Kennett, B. L. N., E. R. Engdahl, and R. Buland (1995), Constraints on seismic velocities in the Earth from traveltimes, *Geophys. J. Int.*, *122*(1), 108–124.

Kent, P. E. (1979), The emergent Hormuz salt plugs of southern Iran, *J. Petr. Geol.*, *2*, 117–144.

Khadivi, S., F. Mouthereau, J.-C. Larrasoaña, J. Vergés, O. Lacombe, E. Khademi, E. Beamud, M. Melinte-Dobrinescu, and J.-P. Suc (2010), Magnetochronology of synorogenic Miocene foreland sediments in the Fars arc of the Zagros Folded Belt (SW Iran), *Basin. Res.*, *22*, 918–932, doi:10.1111/j.1365-2117.2009.00446.x.

Kissling, E. (1988), Geotomography with local earthquake data, *Rev. Geophys.*, *26*, 659–698, doi:10.1029/RG026i004p00659.

Lienert, B. R., and J. Havskov (1995), HYPOCENTER 3.2: A computer program for locating earthquakes locally, regionally and globally, *Seismol. Res. Lett.*, *66*, 26–36.

Lohman, R. B., and W. D. Barnhart (2010), Evaluation of earthquake triggering during the 2005–2008 earthquake sequence on Qeshm Island, Iran, *J. Geophys. Res.*, *115*, B12413, doi:10.1029/2010JB007710.

Lohman, R. B., and M. Simons (2005a), Locations of selected small earthquakes in the Zagros mountains, *Geochem. Geophys. Geosyst.*, *6*, Q03001, doi:10.1029/2004GC000849.

Lohman, R. B., and M. Simons (2005b), Some thoughts on the use of InSAR data to constrain models of surface deformation: Noise structure and data downsampling, *Geochem. Geophys. Geosyst.*, *6*, Q01007, doi:10.1029/2004GC000841.

Masson, F., J. Chéry, D. Hatzfeld, J. Martinod, P. Vernant, F. Tavakoli, and M. Ghafory-Ashtiani (2005), Seismic versus aseismic deformation in Iran inferred from earthquakes and geodetic data, *Geophys. J. Int.*, *160*, 217–226, doi:10.1111/j.1365-246X.2004.02465.x.

McCaffrey, R., and G. Abers (1988), SYN3: A program for inversion of teleseismic body waveforms on microcomputers, Air Force Geophys. Lab. Tech. Rep. AFGL-TR-0099, Hanscomb Air Force Base, Mass.

McCaffrey, R., P. Zwick, and G. Abers (1991), SYN4 Program, Tech. Rep., IASPEI Software Library, Mass. Inst. of Technol., Mass.

McNamara, D. E., H. M. Benz, R. B. Herrmann, E. A. Bergman, P. Earle, A. Meltzer, M. Withers, and M. Chapman (2014), The Mw 5.8 Mineral, Virginia, earthquake of August 2011 and aftershock sequence: Constraints on earthquake source parameters and fault geometry, *Bull. Seismol. Soc. Am.*, *104*, 40–54, doi:10.1785/0120130058.

McQuarrie, N. (2004), Crustal scale geometry of the Zagros fold-thrust belt, Iran, *J. Struct. Geol.*, *26*, 519–535.

McQuarrie, N., and D. J. J. van Hinsbergen (2013), Retrodeforming the Arabia-Eurasia collision zone: Age of collision versus magnitude of continental subduction, *Geology*, *41*(3), 315–318.

Molinaro, M., P. Leturmy, J.-C. Guezou, D. Frizon de Lamotte, and S. A. Eshraghi (2005), The structure and kinematics of the southeastern Zagros fold-thrust belt, Iran: From thin-skinned to thick-skinned tectonics, *Tectonics*, *24*, TC3007, doi:10.1029/2004TC001633.

Mouthereau, F., J. Tensi, N. Bellahsen, O. Lacombe, T. De Boisgrollier, and S. Kargar (2007), Tertiary sequence of deformation in a thin-skinned/thick-skinned collision belt: The Zagros Folded Belt (Fars, Iran), *Tectonics*, *26*, TC5006, doi:10.1029/2007TC002098.

Mouthereau, F., O. Lacombe, and J. Vergés (2012), Building the Zagros collisional orogen: Timing, strain distribution and the dynamics of Arabia/Eurasia plate convergence, *Tectonophysics*, *532*, 27–60.

Nabelek, J. L. (1984), Determination of earthquake source parameters from inversion of body waves, PhD thesis, MIT Dept. of Earth, Atmos. and Planet. Sci., Cambridge, Mass.

Nissen, E., B. Emmerson, G. J. Funning, A. Mistrukov, B. Parsons, D. P. Robinson, E. Rogozhin, and T. J. Wright (2007a), Combining InSAR and seismology to study the 2003 Siberian Altai earthquakes-dextral strike-slip and anticlockwise rotations in the northern India-Eurasia collision zone, *Geophys. J. Int.*, *169*, 216–232, doi:10.1111/j.1365-246X.2006.03286.x.

Nissen, E., M. Ghorashi, J. Jackson, B. Parsons, and M. Talebian (2007b), The 2005 Qeshm Island earthquake (Iran)—A link between buried reverse faulting and surface folding in the Zagros Simply Folded Belt?, *Geophys. J. Int.*, *171*, 326–338, doi:10.1111/j.1365-246X.2007.03514.x.

Nissen, E., F. Yamini-Fard, M. Tatar, A. Gholamzadeh, E. Bergman, J. R. Elliott, J. A. Jackson, and B. Parsons (2010), The vertical separation of mainshock rupture and microseismicity at Qeshm island in the Zagros fold-and-thrust belt, Iran, *Earth Planet. Sci. Lett.*, *296*, 181–194, doi:10.1016/j.epsl.2010.04.049.

Nissen, E., M. Tatar, J. A. Jackson, and M. B. Allen (2011), New views on earthquake faulting in the Zagros fold-and-thrust belt of Iran, *Geophys. J. Int.*, *186*, 928–944, doi:10.1111/j.1365-246X.2011.05119.x.

Nissen, E., J. A. Jackson, S. Jahani, and M. Tatar (2014), Zagros "phantom earthquakes" reassessed—The interplay of seismicity and deep salt flow in the Simply Folded Belt?, *J. Geophys. Res. Solid Earth*, *119*, 3561–3583, doi:10.1002/2013JB010796.

O'Brien, C. A. E. (1957), Salt diapirism in south Persia, *Geologie en Mijnbouw*, *19*, 357–376.

Okada, Y. (1985), Surface deformation due to shear and tensile faults in a half-space, *Bull. Seismol. Soc. Am.*, *75*(4), 1135–1154.

Oveisi, B., J. Lavé, and P. van der Beek (2007), Rates and processes of active folding evidenced by Pleistocene terraces at the central Zagros front (Iran), in *Thrust Belts and Foreland Basins*, pp. 267–287, Springer, Berlin.

Oveisi, B., J. Lavé, P. van der Beek, J. Carcaillet, L. Benedetti, and C. Aubourg (2009), Thick- and thin-skinned deformation rates in the central Zagros simple folded zone (Iran) indicated by displacement of geomorphic surfaces, *Geophys. J. Int.*, *176*, 627–654, doi:10.1111/j.1365-246X.2008.04002.x.

Parsons, B., T. Wright, P. Rowe, J. Andrews, J. Jackson, R. Walker, M. Khatib, M. Talebian, E. Bergman, and E. R. Engdahl (2006), The 1994 Sefidabeh (eastern Iran) earthquakes revisited: New evidence from satellite radar interferometry and carbonate dating about the growth of an active fold above a blind thrust fault, *Geophys. J. Int.*, *164*, 202–217, doi:10.1111/j.1365-246X.2005.02655.x.

Paul, A., A. Kaviani, D. Hatzfeld, J. Vergne, and M. Mokhtari (2006), Seismological evidence for crustal-scale thrusting in the Zagros mountain belt (Iran), *Geophys. J. Int.*, *166*, 227–237, doi:10.1111/j.1365-246X.2006.02920.x.

Perotti, C. R., S. Carruba, M. Rinaldi, G. Bertozzi, L. Feltre, and M. Rahimi (2011), The Qatar-South Fars Arch Development (Arabian Platform, Persian Gulf): Insights from seismic interpretation and analogue modelling, in *New Frontiers in Tectonic Research-At the Midst of Plate Convergence*, edited by U. Schattner, pp. 325–352, InTech., doi:10.5772/20299. [Available at http://www.intechopen.com/books/new-frontiers-in-tectonic-research-at-the-midst-of-plate-convergence/the-qatar-south-fars-arch-development-arabian-platform-persian-gulf-insights-from-seismic-interpreta.]

Press, W. H., S. A. Teukolsky, W. T. Vetterling, and B. P. Flannery (1992), *Numerical Recipes in C: The Art of Scientific Computing*, 2nd ed., Cambridge Univ. Press, Cambridge, U. K.

Reilinger, R., et al. (2006), GPS constraints on continental deformation in the Africa-Arabia-Eurasia continental collision zone and implications for the dynamics of plate interactions, *J. Geophys. Res.*, *111*, B05411, doi:10.1029/2005JB004051.

Roustaei, M., E. Nissen, M. Abbassi, A. Gholamzadeh, M. Ghorashi, M. Tatar, F. Yamini-Fard, E. Bergman, J. Jackson, and B. Parsons (2010), The 2006 March 25 Fin earthquakes (Iran)-insights into the vertical extents of faulting in the Zagros Simply Folded Belt, *Geophys. J. Int.*, *181*, 1275–1291, doi:10.1111/j.1365-246X.2010.04601.x.

Scholz, C. H. (2002), *The Mechanics of Earthquakes and Faulting*, Cambridge Univ. Press, Cambridge, U. K.

Semmane, F., F. Cotton, and M. Campillo (2005), The 2000 Tottori earthquake: A shallow earthquake with no surface rupture and slip properties controlled by depth, *J. Geophys. Res.*, *110*, B03306, doi:10.1029/2004JB003194.

Sepehr, M., J. Cosgrove, and M. Moieni (2006), The impact of cover rock rheology on the style of folding in the Zagros fold-thrust belt, *Tectonophysics*, *427*, 265–281, doi:10.1016/j.tecto.2006.05.021.

Shen, Z.-K., J. Lü, M. Wang, and R. Bürgmann (2005), Contemporary crustal deformation around the southeast borderland of the Tibetan Plateau, *J. Geophys. Res.*, *110*, B11409, doi:10.1029/2004JB003421.

Sherkati, S., J. Letouzey, and D. Frizon de Lamotte (2006), Central Zagros fold-thrust belt (Iran): New insights from seismic data, field observation, and sandbox modeling, *Tectonics*, *25*, TC4007, doi:10.1029/2004TC001766.

Sipkin, S. A. (1982), Estimation of earthquake source parameters by the inversion of waveform data: Synthetic waveforms, *Phys. Earth Planet. Inter.*, *30*(2-3), 242–259, doi:10.1016/0031-9201(82)90111-X.

Takada, Y., T. Kobayashi, M. Furuya, and M. Murakami (2009), Coseismic displacement due to the 2008 Iwate-Miyagi Nairiku earthquake detected by ALOS/PALSAR: Preliminary results, *Earth Planets Space*, *61*, e9–e12.

Talebian, M., and J. Jackson (2004), A reappraisal of earthquake focal mechanisms and active shortening in the Zagros mountains of Iran, *Geophys. J. Int.*, *156*, 506–526, doi:10.1111/j.1365-246X.2004.02092.x.

Tatar, M., D. Hatzfeld, and M. Ghafory-Ashtiany (2004), Tectonics of the Central Zagros (Iran) deduced from microearthquake seismicity, *Geophys. J. Int.*, *156*, 255–266, doi:10.1111/j.1365-246X.2003.02145.x.

Tatar, M., D. Hatzfeld, A. S. Moradi, and A. Paul (2005), The 2003 December 26 Bam earthquake (Iran), Mw 6.6, aftershock sequence, *Geophys. J. Int.*, *163*, 90–105, doi:10.1111/j.1365-246X.2005.02639.x.

Tatar, M., J. Jackson, D. Hatzfeld, and E. Bergman (2007), The 2004 May 28 Baladeh earthquake (M_w 6.2) in the Alborz, Iran: Overthrusting the South Caspian Basin margin, partitioning of oblique convergence and the seismic hazard of Tehran, *Geophys. J. Int.*, *170*, 249–261, doi:10.1111/j.1365-246X.2007.03386.x.

Taymaz, T., H. Eyidoğan, and J. Jackson (1991), Source parameters of large earthquakes in the East Anatolian Fault Zone (Turkey), *Geophys. J. Int.*, *106*, 537–550, doi:10.1111/j.1365-246X.1991.tb06328.x.

Tong, X., D. T. Sandwell, and Y. Fialko (2010), Coseismic slip model of the 2008 Wenchuan earthquake derived from joint inversion of interferometric synthetic aperture radar, GPS, and field data, *J. Geophys. Res.*, *115*, B04314, doi:10.1029/2009JB006625.

Vernant, P., et al. (2004), Present-day crustal deformation and plate kinematics in the Middle East constrained by GPS measurements in Iran and northern Oman, *Geophys. J. Int.*, *157*, 381–398, doi:10.1111/j.1365-246X.2004.02222.x.

Waldhauser, F., and W. L. Ellsworth (2000), A double-difference earthquake location algorithm: Method and application to the Northern Hayward Fault, California, *Bull. Seismol. Soc. Am.*, *90*, 1353–1368, doi:10.1785/0120000006.

Walker, R. T., M. J. Andalibi, M. R. Gheitanchi, J. A. Jackson, S. Karegar, and K. Priestley (2005), Seismological and field observations from the 1990 November 6 Furg (Hormozgan) earthquake: A rare case of surface rupture in the Zagros mountains of Iran, *Geophys. J. Int.*, *163*, 567–579, doi:10.1111/j.1365-246X.2005.02731.x.

Walker, R. T., et al. (2013a), The 2010–2011 South Rigan (Baluchestan) earthquake sequence and its implications for distributed deformation and earthquake hazard in southeast Iran, *Geophys. J. Int.*, *193*(1), 349–374, doi:10.1093/gji/ggs109.

Walker, R. T., M. M. Khatib, A. Bahroudi, A. Rodes, C. Schnabel, M. Fattahi, M. Talebian, and E. Bergman (2013b), Co-seismic, geomorphic, and geologic fold growth associated with the 1978 Tabas-e-Golshan earthquake fault in eastern Iran, *Geomorphology*, *237*, 98–118.

Walpersdorf, A., D. Hatzfeld, H. Nankali, F. Tavakoli, F. Nilforoushan, M. Tatar, P. Vernant, J. Chéry, and F. Masson (2006), Difference in the GPS deformation pattern of North and Central Zagros (Iran), *Geophys. J. Int.*, *167*, 1077–1088, doi:10.1111/j.1365-246X.2006.03147.x.

Wells, D. L., and K. J. Coppersmith (1994), New empirical relationships among magnitude, rupture length, rupture width, rupture area, and surface displacement, *Bull. Seismol. Soc. Am.*, *84*(4), 974–1002.

Wessel, P., and W. H. F. Smith (1998), New, improved version of generic mapping tools released, *Eos Trans. AGU*, *79*, 579–579, doi:10.1029/98EO00426.

Wright, T. J., B. E. Parsons, J. A. Jackson, M. Haynes, E. J. Fielding, P. C. England, and P. J. Clarke (1999), Source parameters of the 1 October 1995 Dinar (Turkey) earthquake from SAR interferometry and seismic bodywave modelling, *Earth Planet. Sci. Lett.*, *172*, 23–37, doi:10.1016/S0012-821X(99)00186-7.

Wright, T. J., Z. Lu, and C. Wicks (2003), Source model for the M_w 6.7, 23 October 2002, Nenana Mountain Earthquake (Alaska) from InSAR, *Geophys. Res. Lett.*, *30*, 1974, doi:10.1029/2003GL018014.

Wright, T. J., Z. Lu, and C. Wicks (2004), Constraining the slip distribution and fault geometry of the Mw 7.9, 3 November 2002, Denali fault earthquake with interferometric synthetic aperture radar and global positioning system data, *Bull. Seismol. Soc. Am.*, *94*(6B), S175–189, doi:10.1785/0120040623.

Wright, T. J., J. R. Elliott, H. Wang, and I. Ryder (2013), Earthquake cycle deformation and the Moho: Implications for the rheology of continental lithosphere, *Tectonophysics*, *609*, 504–523, doi:10.1016/j.tecto.2013.07.029.

Yamato, P., B. J. P. Kaus, F. Mouthereau, and S. Castelltort (2011), Dynamic constraints on the crustal-scale rheology of the Zagros fold belt, Iran, *Geology*, *39*(9), 815–818.

Yamini-Fard, F., D. Hatzfeld, M. Tatar, and M. Mokhtari (2006), Microearthquake seismicity at the intersection between the Kazerun fault and the Main Recent Fault (Zagros, Iran), *Geophys. J. Int.*, *166*, 186–196, doi:10.1111/j.1365-246X.2006.02891.x.

Yaminifard, F., M. Tatar, K. Hessami, A. Gholamzadeh, and E. A. Bergman (2012), Aftershock analysis of the 2005 November 27 (Mw 5.8) Qeshm Island earthquake (Zagros-Iran): Triggering of strike-slip faults at the basement, *J. Geodyn.*, *61*, 138–147, doi:10.1016/j.jog.2012.04.005.

Zanjani, A. A., A. Ghods, E. Bergman, G. Mortezanejad, K. Priestley, S. Madanipour, and A. Rezaeian (2013), Seismicity in the western coast of the South Caspian Basin and the Talesh Mountains, *Geophys. J. Int.*, *195*, 799–814, doi:10.1093/gji/ggt299.

Zwick, P., R. McCaffrey, and G. Abers (1994), MT5 Program, in *Bibliographic References and BSSA Database (August, 1994)*, vol. 4, IASPEI Software Library. [Available at http://www.iaspei.org/.]